Asymptotic preserving IMEX finite volume schemes for low Mach number Euler equations with gravitation.

Georgij Bispen, Mária Lukáčová-Medviďová,* Leonid Yelash

Abstract

In this paper we will present and analyse a new class of the IMEX finite volume schemes for the Euler equations with a gravity source term. We will in particular concentrate on a singular limit of weakly compressible flows when the Mach number $M \ll 1$. In order to efficiently resolve slow dynamics we split the whole nonlinear system in a stiff linear part governing the acoustic and gravity waves and a non-stiff nonlinear part that models nonlinear advection effects. For time discretization we use a special class of the so-called globally stiffly accurate IMEX schemes and approximate the stiff linear operator implicitly and the non-stiff nonlinear operator explicitly. For spatial discretization the finite volume approximation is used with the central and Rusanov/Lax-Friedrichs numerical fluxes for the linear and nonlinear subsystem, respectively. In the case of a constant background potential temperature we prove theoretically that the method is asymptotically consistent and asymptotically stable uniformly with respect to small Mach number. We also analyse experimentally convergence rates in the singular limit when the Mach number tends to zero.

Key words: finite volume methods, weakly compressible flows, low Mach number flows, IMEX schemes, asymptotic preserving schemes, asymptotic stability, multiscale analysis

AMS Subject Classification: 35L65, 76B15, 65M08, 65M06, 35L45, 35L65

1 Introduction

In this paper we present new asymptotic preserving implicit-explicit (IMEX) finite volume (FV) schemes for the Euler equations with gravitation. In the case of weakly compressible flows the magnitude of flow velocity $\mathbf{u}$ is much smaller than the sound speed c, which results in the so-called low Mach number flows. Here the Mach number is a reference number defined as $M = \frac{|\mathbf{u}|}{c}$. Such flows arise in many applications, such as meteorology, combustion or astrophysics. We refer also to theoretical works on singular limits of compressible flows, cf. [30, 18, 19]. Development of efficient and stable numerical schemes for weakly compressible flows is a challenging task. In the literature we can find already several studies on this topic. In [6] Bijl and Wesseling have developed a scheme suitable to compute large range of Mach numbers which is based on the finite difference MAC-type scheme for incompressible Euler equations. This approach has been further generalized in [26] and a conservative scheme using the pressure-correction and staggered grid approach (as in the case of the MAC scheme) has been derived and analysed. Another approach, where a numerical scheme for incompressible flows, the so-called SIMPLE

*Institute of Mathematics, Johannes Gutenberg-University Mainz, (bispeng@uni-mainz.de, lukacova@uni-mainz.de, yelash@uni-mainz.de).

method, has been extended to weakly compressible flows, has been developed by Munz, Roller, Klein and Geratz in [41]. In this work the formal asymptotic analysis with respect to small Mach number has been used to gain insight into the limit behavior of the compressible flow equations as the Mach number vanishes. Consequently, multiple pressure variables are introduced into the numerical framework, which allowed accurate capturing of various physical phenomena on very different length scales, see also [45] for further developments. Recently, there has been an interesting approach to approximate all Mach numbers flows derived by Feistauer et al. [20, 21], that is based on the higher order discontinuous Galerkin method. We refer also to a large variety of the so-called sound-proof models, that are used for low Mach number atmospheric flows, see, e.g., Klein et al. [35], Smolarkiewicz et al. [49], Benacchio et al. [5] and the references therein. These models suppress sound waves entirely and provide good approximations for small- to meso-scale atmospheric motions.

On the other hand, there are approaches that generalize numerical schemes developed for compressible flows in order to obtain accurate and stable methods for weakly compressible flows, see, e.g., [31, 25, 17, 8, 46, 42]. Inspired by these works, in our recent paper [43] we have split the flux into the stiff/non-stiff parts and applied implicit/explicit time discretization, that yields a nonlinear elliptic equation for the pressure updates. This acts similarly to a classical incompressible pressure projection algorithm. Unfortunately, the Jacobian of the stiff flux function degenerated in the limit as the Mach number approached zero and a suitable stabilization was needed. Thus, it implied that the spatial and the temporal grid sizes, Δx and Δt, had to be reduced simultaneously as the Mach number $M \to 0$. Consequently, the resulting scheme was only *weakly asymptotic preserving*. The concept of the so-called *asymptotic preserving schemes* has been introduced by Jin et al., see [25], [28] and the references therein; a numerical scheme is called asymptotic preserving if it is uniformly consistent as a singular limit parameter, e.g. the Mach number, approaches its limit. In particular, the scheme reduces to a consistent approximation of the limit equation. We recall that the semi-implicit time discretization has been also used in meteorological applications, see, e.g., [23], [46], [49], [51] to name just a few.

The aim of our paper is to present and analyse new IMEX FV schemes for the Euler equations with the gravity source that are based on acoustic/advection splitting strategy. More precisely, we split the whole nonlinear system of the Euler equations into a stiff linear part governing fast acoustic and gravity waves and a non-stiff nonlinear part that models slow nonlinear advection effects, see also our recent papers [7, 8, 9, 40]. For time discretization we use higher order globally stiffly accurate IMEX schemes and approximate the stiff linear operator implicitly and the non-stiff nonlinear operator explicitly. Consequently, we can efficiently resolve slow nonlinear dynamics due to advection effects. Our goal is to study asymptotic preserving properties of these methods and to show that a suitable splitting into the linear stiff subsystem for acoustic/gravity waves and the nonlinear non-stiff subsystem for the advection combined with the IMEX FV discretization yields asymptotic preserving schemes. In a particular case when the background potential temperature is constant, we will prove their asymptotic consistency that holds uniformly with respect to M. For the Euler equations without the gravitational source term we also prove asymptotic stability of the IMEX FV methods. Furthermore, we analyse experimentally the asymptotic convergence rates in the singular limit as $M \to 0$ and demonstrate that our IMEX FV schemes become consistent discretizations of the limiting equations for anelastic equations in the limit of $M \to 0$. We also refer to a recent work of Kaiser et al.[29], where asymptotic consistency of the so-called RS IMEX schemes for the isentropic Euler equations has been studied. Note that RS IMEX schemes are strongly related to our IMEX FV schemes; both IMEX methods use analogous splitting and may differ in the choice of a reference solution or an equilibrium solution. In [7, 8] we have analysed asymptotic consistency and accuracy of the IMEX FV for the shallow water equations with a bottom topography source term.

In order to preserve equilibria of the underlying hyperbolic balance laws on the discrete level a special treatment of zero-order source terms is required, which yields the well-balanced schemes, see, e.g., [10], [4], [11], [37]. In context of the Euler equations with the gravity source term we refer a reader to Botta et al. [10], where the concept of the so-called hydrostatic reconstruction has been firstly proposed; see also [12], [13]. The schemes presented in our paper are *well-balanced*. Indeed, they preserve a particular underlying equilibrium by the construction, cf. Remark 5.5.

The paper is organized in the following way. In Section 2 we present the mathematical model for weakly compressible flows. The IMEX FV schemes based on a suitable splitting of linearized acoustic waves and the nonlinear advection are introduced in Section 3. In Sections 4 and 5 we study asymptotic preserving properties of our IMEX schemes; we show that they are asymptotically consistent and asymptotically stable with respect to the Mach number M. Numerical experiments presented in Section 6 demonstrate asymptotic preserving properties of the IMEX FV schemes based on the acoustic/advection splitting.

2 Euler equations

Time evolution of three-dimensional inviscid compressible flows is governed by the Euler equations, which express the basic conservation laws: conservation of mass, momentum and energy. In atmospheric applications it is often more suitable to express the energy equation in terms of the potential temperature, see, e.g., [5], [22], [32], [33], [36], [42], [49], [52], and the references therein. We note that for smooth flows both formulations are equivalent.

$$\begin{aligned} \partial_t \rho + \nabla \cdot (\rho \mathbf{u}) &= 0 \\ \partial_t (\rho \mathbf{u}) + \nabla \cdot (\rho \mathbf{u} \otimes \mathbf{u}) + \nabla p &= -\rho g \mathbf{e}_3 \equiv -\rho g \begin{pmatrix} 0 \\ 0 \\ 1 \end{pmatrix} \\ \partial_t (\rho \theta) + \nabla \cdot (\rho \theta \mathbf{u}) &= 0, \end{aligned} \tag{1}$$

where ρ denotes the density, $\mathbf{u}$ velocity vector, p pressure and g the gravitational acceleration. Equation $(1)_3$ may also be interpreted as the first law of thermodynamics for an adiabatic fluid. Denoting T the temperature, the potential temperature θ can be obtained from the equation of an adiabatic process in an ideal gas

$$\theta = T \left(\frac{p_0}{p} \right)^{R/c_p}, \ R = c_p - c_v \text{ is the specific gas constant.}$$

In order to close the system we determine the pressure from the state equation

$$p = p_0 \left(\frac{R \rho \theta}{p_0} \right)^{\gamma}, \tag{2}$$

where $\gamma = c_p/c_v$ is the adiabatic constant and $p_0 = 10^5 Pa$ is a given reference pressure at sea level.

In practical applications there is often an underlying equilibrium background state and the dynamics of interest is governed by (small) perturbations of this equilibrium state. For example, in meteorological applications it is the hydrostatic equilibrium that expresses a balance between the gravity and pressure forces. Let $\bar{p}$, $\bar{\rho}$, $\bar{\mathbf{u}}(= 0)$, $\bar{\theta}$, $\overline{\rho\theta}$ denote the pressure, density, velocity, potential temperature and energy for the hydrostatic equilibrium, i.e.

$$\partial_{x_3} \bar{p} = -\bar{\rho} g. \tag{3}$$

Furthermore, let $\rho', p', \mathbf{u}', \theta', (\rho\theta)'$ stand for the corresponding perturbations of the background states. Thus, we have $\rho = \bar{\rho}+\rho'$, $p = \bar{p}+p'$, $\theta = \bar{\theta}+\theta'$, and $(\rho\theta) = \overline{\rho\theta}+\bar{\rho}\theta'+\rho'\bar{\theta}+\rho'\theta' \equiv \overline{\rho\theta}+(\rho\theta)'$. Since with the background state $\bar{\mathbf{u}} = 0$, the velocity $\mathbf{u} = \bar{\mathbf{u}} + \mathbf{u}'$ ($\mathbf{u} \in \mathbb{R}^3$) becomes $\mathbf{u} \equiv \mathbf{u}'$, we will omit the prime symbol hereinafter.

In order to avoid numerical instabilities due to the round-off errors and the multiscale behaviour of the Euler equations in the case of low Mach number limit, the numerical simulations are typically realized for the perturbations, which satisfy the following equations

$$\begin{aligned} &\partial_t \rho' + \nabla \cdot (\rho \mathbf{u}) = 0 \\ &\partial_t (\rho \mathbf{u}) + \nabla \cdot (\rho \mathbf{u} \otimes \mathbf{u}) + \nabla p' = -\rho' g \mathbf{e}_3 \\ &\partial_t (\rho\theta)' + \nabla \cdot (\rho\theta \mathbf{u}) = 0. \end{aligned} \tag{4}$$

The Pressure perturbation p' can be expressed from the state equation (2), i.e. $p' = p - \bar{p} = = p_0 \left(\frac{R}{p_0}\right)^{\gamma} ((\rho\theta)^{\gamma} - (\overline{\rho\theta})^{\gamma})$.

We apply the standard non-dimensionalisation with a reference length x_{ref}, time scale t_{ref}, reference flow velocity u_{ref}, reference density ρ_{ref} and reference pressure p_{ref}. Let the reference sound speed $c_{ref} := \sqrt{\gamma p_{ref}/\rho_{ref}}$ and $u_{ref} t_{ref} = x_{ref}$. Then the Mach and Froude numbers read

$$M = \frac{u_{ref}}{c_{ref}}, \quad Fr = \frac{u_{ref}}{\sqrt{g x_{ref}}}. \tag{5}$$

We assume that $\gamma M^2 = Fr^2$. Denoting a small parameter $\varepsilon = \sqrt{\gamma} M = Fr$, the Euler equations for the perturbed variables (4) can be rewritten equivalently in the non-dimensional form

$$\begin{aligned} \partial_t \rho' + \nabla \cdot (\rho \mathbf{u}) &= 0 \\ \partial_t (\rho \mathbf{u}) + \nabla \cdot (\rho \mathbf{u} \otimes \mathbf{u}) + \frac{1}{\varepsilon^2} \nabla p' &= -\frac{1}{\varepsilon^2} \rho' \mathbf{e}_3 \\ \partial_t (\rho\theta)' + \nabla \cdot (\rho\theta \mathbf{u}) &= 0. \end{aligned} \tag{6}$$

In the above non-dimensionalization procedure we have considered only one type of gravity waves, that are called the external (barotropic) gravity waves in the meteorological literature. In more detailed atmospheric models the internal gravity waves have to be considered as well. This yields another characteristic number, the internal Froude number $Fr_{int} = Fr \frac{1}{\sqrt{x_{ref} \partial_{x_3} \theta/\theta}}$; $M \approx Fr \ll Fr_{int} \ll 1$. We refer a reader to [34], where a nice overview of various sound-proof models used in the meteorological literature and detailed asymptotic analysis are presented, see also [32], [33], [35].

Remark 2.1 *Let the background potential temperature be $\bar{\theta} = const.$ and the background density at sea level be $\bar{\rho}(0) \equiv \rho_0 = p_0/R\bar{\theta}$. Then we have an explicit expression for the background hydrostatic equilibrium state*

$$\bar{\rho}(x_3) = \frac{1}{\bar{\theta}} \left(1 - \frac{(\gamma-1)x_3}{\gamma \bar{\theta}}\right)^{\frac{1}{\gamma-1}}, \quad \bar{p}(x_3) = (\bar{\rho}(x_3)\bar{\theta})^{\gamma}.$$

Indeed, using the non-dimensional form of (3), $\bar{p}_{x_3} = \bar{\rho}$, and the state equation $\bar{p} = (\overline{\rho\theta})^{\gamma}$ we have the following ordinary differential equation

$$(\overline{\rho\theta})^{\gamma-1} \frac{d(\overline{\rho\theta})}{dx_3} = -\frac{1}{\gamma} \bar{\rho} \tag{7}$$

with $\bar{\rho}(0) = \rho_0$. Since $\bar{\theta} = const.$ we obtain the ordinary differential equation for density

$$\frac{\bar{\theta}^\gamma}{\gamma - 1} \frac{d\rho^{\gamma-1}}{dx_3} = \bar{\theta}^\gamma \bar{\rho}^{\gamma-2} \frac{d\bar{\rho}}{dx_3} = -\frac{1}{\gamma}, \tag{8}$$

which has a unique solution

$$\bar{\rho} = \frac{1}{\bar{\theta}} \left(1 - \frac{(\gamma-1)x_3}{\gamma\bar{\theta}}\right)^{\frac{1}{\gamma-1}}.$$

The background state for pressure is obtained from the non-dimensional form of the state equation $\bar{p} = (\overline{\rho\theta})^\gamma$. This result can be generalized also for stratified potential temperature, i.e. non-constant $\bar{\theta}$ with $\frac{1}{\bar{\theta}} \frac{d\bar{\theta}}{dx_3} = \mathcal{O}(\varepsilon^2)$. The hydrostatic distribution for $\bar{\rho}(x_3)$ and $\bar{p}(x_3)$ then reads [33]

$$\bar{\rho}(x_3) = \frac{1}{\bar{\theta}(x_3)} \left(1 - \frac{\gamma-1}{\gamma} \int_0^{x_3} \frac{1}{\bar{\theta}(z)} dz\right)^{\frac{1}{\gamma-1}}, \qquad \bar{p}(x_3) = \left(\bar{\rho}(x_3)\bar{\theta}(x_3)\right)^\gamma.$$

Remark 2.2 *Using the dimensional formulation the above background hydrostatic equilibrium reads*

$$\bar{\rho} = \frac{p_0}{R\bar{\theta}} \pi_e^{\frac{1}{\gamma-1}}, \qquad \bar{p} = p_0 \left(\frac{R\overline{\rho\theta}}{p_0}\right)^\gamma, \tag{9}$$

where $\pi_e = 1 - g/(c_p \int_0^{x_3} \frac{1}{\theta(z)} dz)$ is the so-called Exner pressure.

Remark 2.3 *In order to analyse multiscale effects of the underlying equations it is often advisable to apply a formal asymptotic analysis and express all variables in the form of the Hilbert expansion*

$$f = f^{(0)} + \varepsilon f^{(1)} + \varepsilon^2 f^{(2)}. \tag{10}$$

We substitute this expansion into a non-dimensional form of the Euler equations (1) and compare the equal order terms in ε. Assuming that $\theta^{(0)} = const.$ the limit equations of (6) read

$$\nabla \cdot (\rho^{(0)}\mathbf{u}^{(0)}) = 0, \quad \partial_t(\rho^{(0)}\mathbf{u}^{(0)}) + \nabla \cdot \left(\rho^{(0)}\mathbf{u}^{(0)} \otimes \mathbf{u}^{(0)}\right) + \nabla p^{(2)} = -\rho^{(2)}\mathbf{e}_3, \tag{11}$$

$$\partial_t \theta^{(2)} + \mathbf{u}^{(0)} \cdot \nabla\theta^{(2)} = 0, \tag{12}$$

which are the incompressible Euler equations for fluids with variable density and the transport equation for potential temperature. Note that in the case of hydrostatic equilibrium state we obtain using (3) and (1) $\bar{\rho} = \rho^{(0)}$, $\bar{p} = p^{(0)}$, $\bar{\theta} = \theta^{(0)}$, $\rho' = \varepsilon^2\rho^{(2)}$, $p' = \varepsilon^2 p^{(2)}$, $\theta' = \varepsilon^2\theta^{(2)}$.

Following [31], [52], [19] we can rewrite the momentum equation (11) as

$$\partial_t \mathbf{u}^{(0)} + \mathbf{u}^{(0)} \cdot \nabla\mathbf{u}^{(0)} + \frac{1}{\rho^{(0)}} \nabla p^{(2)} = \theta^{(2)}\mathbf{e}_3. \tag{13}$$

In the meteorological literature equations $(11)_1$, (13), (12) are called the anelastic model equations, see Ogura and Philipps [44].

3 Numerical schemes

Our asymptotic preserving FV schemes are based on the following acoustic/advection splitting of the Euler equations into a linear $\mathcal{L}$ and nonlinear $\mathcal{N}$ part, respectively, see also [46], [40] and the references therein for further details. To this end let us rewrite (4) in the following compact form. Let $\mathbf{w} = (\rho', \rho\mathbf{u}, \rho\theta')^T$, $\mathbf{F} = (\rho\mathbf{u}, \rho\mathbf{u} \otimes \mathbf{u} + \frac{1}{\varepsilon^2} p' \mathbb{1}, \rho\theta\mathbf{u})^T$, $\mathbb{1} \in \mathbb{R}^{3\times 3}$ is the identity matrix, $S = (0, -\frac{1}{\varepsilon^2}\rho'\mathbf{e}_3, 0)^T$, then (6) can be written as

$$\frac{\partial \mathbf{w}}{\partial t} = -\nabla \cdot \mathbf{F}(\mathbf{w}) + \mathbf{S}(\mathbf{w}) = \mathcal{L}(\mathbf{w}) + \mathcal{N}(\mathbf{w}). \tag{14}$$

We would like to point out that the choice of the linear and nonlinear operators, $\mathcal{L}$ and $\mathcal{N}$, respectively, is crucial. Indeed, we choose $\mathcal{L}$ to model linear acoustic and gravity waves, whereas the operator $\mathcal{N}$ describes resulting nonlinear advective/convective effects. Analogously as in [40] we set

$$\mathcal{L}(\mathbf{w}) \equiv -\nabla \cdot \mathcal{F}_L(\mathbf{w}) + S(\mathbf{w}) := -\begin{pmatrix} \nabla \cdot (\rho\mathbf{u}) \\ \frac{1}{\varepsilon^2}\partial p'/\partial x_1 \\ \frac{1}{\varepsilon^2}\partial p'/\partial x_2 \\ \frac{1}{\varepsilon^2}\partial p'/\partial x_3 + \frac{1}{\varepsilon^2}\rho' \\ \nabla \cdot (\overline{\theta}\rho\mathbf{u}) \end{pmatrix} \tag{15}$$

with the linearized pressure $p' \approx p'_L \equiv \frac{\bar{c}^2}{\overline{\theta}}(\rho\theta)'$ and

$$\mathcal{N} \equiv -\nabla \cdot \mathcal{F}_N(\mathbf{w}) := -\nabla \cdot \begin{pmatrix} 0 \\ \rho\mathbf{u} \otimes \mathbf{u} \\ \theta'\rho\mathbf{u} \end{pmatrix}. \tag{16}$$

Realizing that $\bar{\theta} = \overline{\rho\theta}/\bar{\rho}$ the linearized pressure p'_L has been obtained by applying the Taylor expansion in the expression for p' with respect to $\overline{\rho\theta}$. Thus, we have $p' = (\rho\theta)^\gamma - (\overline{\rho\theta})^\gamma$, $p' = p'_L + p'_{NL}$, where

$$p'_L = \frac{\bar{c}^2}{\overline{\theta}}(\rho\theta)' \text{ with } \bar{c} = \sqrt{\frac{\gamma\bar{p}}{\bar{\rho}}} \text{ and } p'_{NL} = p' - p'_L = \mathcal{O}(((\rho\theta)')^2). \tag{17}$$

In the nonlinear operator $\mathcal{N}$ one may also include the nonlinear pressure perturbation $p'_{NL} = \mathcal{O}(\varepsilon^4)$. However, in order to simplify the eigenstructure of $\mathcal{N}$ and to keep the operator hyperbolic it is suitable to omit p'_{NL}. Our extensive numerical experiments demonstrate that both approaches with/without p'_{NL} yield similar results in the low Mach number limit. It is worthwhile to point out that the linear flux leads to the stiff subsystem

$$\frac{\partial \mathbf{w}}{\partial t} = -\nabla \cdot \mathcal{F}_L(\mathbf{w}) \tag{18}$$

having the eigenvalues $\lambda_1 = -\frac{\bar{c}}{\varepsilon}, \lambda_2 = \lambda_3 = \lambda_4 = 0, \lambda_5 = \frac{\bar{c}}{\varepsilon}, \bar{c} = \sqrt{\gamma\bar{p}/\bar{\rho}}$. Note, that the internal gravity waves do not arise as a linear mode in our linearized analysis. The external gravity waves are treated as a source term. On the other hand the nonlinear subsystem

$$\frac{\partial \mathbf{w}}{\partial t} = -\nabla \cdot \mathcal{F}_{NL}(\mathbf{w}) \tag{19}$$

is non-stiff and its eigenvalues are $\lambda_1 = 0, \lambda_2 = \lambda_3 = \lambda_4 = \mathbf{u} \cdot \mathbf{n}, \lambda_5 = 2\mathbf{u} \cdot \mathbf{n}$, where $\mathbf{n} \in \mathbb{R}^3$ is an arbitrary unit vector.

Consequently, we will discretize the Euler equations by the IMEX scheme in time and approximate the linear stiff system at a new time level t_{n+1} and the nonlinear one at the old time level t_n. This yields the first order IMEX scheme

$$\mathbf{w}^{n+1} = \mathbf{w}^n + \Delta t \mathcal{L}(\mathbf{w}^{n+1}) + \Delta t \mathcal{N}(\mathbf{w}^n). \tag{20}$$

In order to increase the accuracy we will apply the second order IMEX schemes. One possibility is to apply the second order BDF scheme, cf. [3], [46], [47]

$$\mathbf{w}^{n+1} = \alpha_0 \mathbf{w}^n + \alpha_1 \mathbf{w}^{n-1} \beta \mathcal{L}(\mathbf{w}^{n+1}) + \beta_0 \mathcal{N}(\mathbf{w}^n) + \beta_1 \mathcal{N}(\mathbf{w}^{n-1}), \tag{21}$$

$\alpha_0 = \frac{4}{3};\ \alpha_1 = -\frac{1}{3};\ \beta = \frac{2}{3}\Delta t;\ \beta_0 = \frac{4}{3}\Delta t;\ \beta_1 = -\frac{2}{3}\Delta t.$

Another option is to apply the globally stiffly accurate second order IMEX scheme. A suitable candidate is the so-called ARS(2,2,2) scheme derived by Asher, Ruuth and Spiteri in [2].

$$\begin{aligned} \mathbf{w}^{n+1/2} &= \mathbf{w}^n + \Delta t \alpha [\mathcal{L}(\mathbf{w}^{n+1/2}) + \mathcal{N}(\mathbf{w}^n)] \\ \mathbf{w}^{n+1} &= \mathbf{w}^n + \Delta t [\delta \mathcal{N}(\mathbf{w}^n) + (1-\delta)\mathcal{N}(\mathbf{w}^{n+1/2})] + \Delta t \alpha \mathcal{L}(\mathbf{w}^{n+1}) + \Delta t (1-\alpha)\mathcal{L}(\mathbf{w}^{n+1/2}), \end{aligned} \tag{22}$$

where $\alpha = 1 - 1/\sqrt{2};\ \delta = 1 - 1/(2\alpha)$.

Spatial discretization is realized by the finite volume scheme. In particular, having a regular rectangular grid we approximate the corresponding divergence operators by applying the numerical flux functions in order to approximate fluxes along the cell interfaces. Let us denote the finite difference in the x_1 direction at the mesh cell $\Omega_{i,j,m} \equiv [x_i - \Delta x_1/2, x_i + \Delta x_1/2] \times [y_j - \Delta x_2/2, y_j + \Delta x_2/2] \times [z_m - \Delta x_3/2, z_m + \Delta x_3/2]$ by $\delta_{x_1} f_{ijm} \equiv f_{i+1/2,j,m} - f_{i-1/2,j,m}$, $f_{i+1/2} := (f_{i+1} + f_i)/2$; an analogous notation holds in the x_2 and x_3 directions. The finite volume discretization of the operators $\mathcal{L}$ and $\mathcal{N}$ yields

$$\begin{aligned} \mathcal{L}(\mathbf{w}^\ell) &= -\sum_{i,j,m} \sum_{k=1}^{3} \frac{1}{\Delta x_k} \delta_{x_k} \mathcal{H}_L(\mathbf{w}^\ell)_{ijm} + S(\mathbf{w}^\ell)_{ijm}, \quad \ell = n+1, n+1/2 \\ \mathcal{N}(\mathbf{w}^\ell) &= -\sum_{i,j,m} \sum_{k=1}^{3} \frac{1}{\Delta x_k} \delta_{x_k} \mathcal{H}_N(\mathbf{w}^\ell)_{ijm}, \qquad \ell = n, n-1, n+1/2, \end{aligned} \tag{23}$$

where $\mathcal{H}_L$ and $\mathcal{H}_N$ denote suitable numerical fluxes for the linear and nonlinear operators, respectively.

For the nonlinear subsystem we have applied, e.g., the Lax-Friedrichs or the Rusanov numerical flux, but any standard numerical flux yielding a stable approximation can be used as well. For example, the Lax-Friedrichs or the Rusanov flux applied in the x_1-direction gives

$$\mathcal{H}_N(\mathbf{w}^\ell)_{i+1/2,j,m} = \frac{1}{2}\left(\mathcal{F}_N(\mathbf{w}^\ell_{i+1,j,m}) + \mathcal{F}_N(\mathbf{w}^\ell_{i,j,m}) - \frac{1}{\lambda}(\mathbf{w}^\ell_{i+1,j,m} - \mathbf{w}^\ell_{i,j,m}) \right) \tag{24}$$

with $\lambda = \Delta t/\Delta x_1$ for the Lax-Friedrichs scheme. For the Rusanov scheme we have $\lambda = \max(\lambda_{\mathbf{w}^\ell_{i+1,j,m}}, \lambda_{\mathbf{w}^\ell_{i,j,m}})$, which is the maximal local eigenvalues of the Jacobian matrix corresponding to (16), that is frozen either in the right $\mathbf{w}^\ell_{i+1,j,m}$ or the left $\mathbf{w}^\ell_{i,j,m}$ approximate solution. In order to keep the explicit finite volume approximation of the nonlinear subsystem stable, we need to fulfill the Courant-Friedrichs-Lewy stability condition. In our numerical experiments we have denoted by

$$CFL_u \equiv \max_{s=1,2,3} \max_{i,j,m} |(\mathbf{u}_s)_{ijm}| \frac{\Delta t}{\Delta x_s} \tag{25}$$

and set $CFL_u < 0.5$ instead of the stability condition required by fully explicit schemes, i.e.

$$CFL \equiv \max_{s=1,2,3} \max_{i,j,m} (|(\mathbf{u}_s)_{ijm}| + c) \frac{\Delta t}{\Delta x_s} \leq 1. \tag{26}$$

In case of the linear subsystem it is suitable to choose central differences, which will yield asymptotic preserving schemes, cf. Section 4,

$$\mathcal{H}_L(\mathbf{w}^\ell)_{i+1/2,j,m} = \frac{1}{2} \left(\mathcal{F}_L(\mathbf{w}^\ell_{i+1,j,m}) + \mathcal{F}_L(\mathbf{w}^\ell_{i,j,m}) \right). \tag{27}$$

Analogous notation holds in the x_2, x_3-directions.

Application of the central differences leads directly to the second order spatial approximation. For the nonlinear subsystem the second order spatial discretization is obtained via MUSCL-type approach using a linear reconstruction in space. We refer a reader to, e.g., [8] for further details. In what follows we will analyse the above IMEX FV schemes both from the analytical as well as experimental point of view.

4 Asymptotic preserving properties: consistency

The aim of this section is to analyse the asymptotic preserving properties of the derived IMEX FV schemes. We will show firstly that the schemes yield consistent approximation of the limiting equations and in the limit as $\varepsilon \to 0$ become an approximation of the anelastic equation (43). We will confine ourselves with the IMEX first order scheme; in an analogous way the generalization for the BDF2 and ARS(2,2,2) second order schemes can be derived, see [7]. For the space discretization numerical fluxes (24) and (27) are applied for the explicit and implicit parts, respectively. Using the matrix-vector notation we can rewrite first order IMEX FV method (20), (23), (24), (27) in the following form

$$M\mathbf{W}^{n+1} = \hat{\mathbf{W}}, \quad M := \mathbb{1} + \Delta t A, \tag{28}$$

where $\mathbb{1} \in \mathbb{R}^{5N \times 5N}$ denotes the identity matrix, N is the number of mesh cells, $\mathbf{W}^{n+1} \equiv \equiv (\boldsymbol{\rho}', \mathbf{Q}_1, \mathbf{Q}_2, \mathbf{Q}_3, (\boldsymbol{\rho\theta})')^{n+1} \in \mathbb{R}^{5N}$ the solution vector at the new time step and $\hat{\mathbf{W}} \equiv \equiv (\hat{\boldsymbol{\rho}}', \hat{\mathbf{Q}}_1, \hat{\mathbf{Q}}_2, \hat{\mathbf{Q}}_3, \widehat{(\boldsymbol{\rho\theta})'}) \in \mathbb{R}^{5N}$ is the vector representing the explicit terms. Further, the matrix A is the matrix arising from the central difference approximation of the linear operator $\mathcal{L}$ in space, cf. (27)

$$A := \begin{bmatrix} 0 & \mathfrak{D}_{x_1} & \mathfrak{D}_{x_2} & \mathfrak{D}_{x_3} & 0 \\ 0 & 0 & 0 & 0 & \frac{1}{\varepsilon^2}\mathfrak{D}_{x_1}\bar{C}^2\bar{\Theta}^{-1} \\ 0 & 0 & 0 & 0 & \frac{1}{\varepsilon^2}\mathfrak{D}_{x_2}\bar{C}^2\bar{\Theta}^{-1} \\ \mathbb{1}/\varepsilon^2 & 0 & 0 & 0 & \frac{1}{\varepsilon^2}\mathfrak{D}_{x_3}\bar{C}^2\bar{\Theta}^{-1} \\ 0 & \mathfrak{D}_{x_1}\bar{\Theta} & \mathfrak{D}_{x_2}\bar{\Theta} & \mathfrak{D}_{x_3}\bar{\Theta} & 0 \end{bmatrix}, \tag{29}$$

where $\bar{C}^2 \in \mathbb{R}^{N \times N}$ is the diagonal matrix representing the known function $\bar{c}^2$. If we assume that the background potential temperature $\bar{\theta} = \text{const.}$ we have $\bar{\Theta}^{-1} = \mathbb{1}/\bar{\theta}$, otherwise $\bar{\Theta}^{-1} \in \mathbb{R}^{N \times N}$ is a diagonal matrix. Further, $\mathfrak{D}_{x_s} \in \mathbb{R}^{N \times N}$ represents a block matrix arising from the central differences $\delta_{x_s} f/(2\Delta x_s)$, $s = 1, 2, 3$. We apply the Gauss elimination to reduce the system and remove the momentum from the linear equations of density and potential temperature. This

yields us the following system

$$(\mathbb{1} + \Delta t^2 B)\begin{pmatrix} \boldsymbol{\rho}' \\ (\boldsymbol{\rho\theta})' \end{pmatrix}^{n+1} = \begin{pmatrix} \hat{\boldsymbol{\rho}}' - \Delta t \nabla_h \cdot \hat{\mathbf{Q}} \\ \widehat{(\boldsymbol{\rho\theta})}' - \Delta t \nabla_h \cdot (\bar{\Theta}\hat{\mathbf{Q}}) \end{pmatrix}, \tag{30a}$$

$$B := \begin{bmatrix} -\frac{1}{\varepsilon^2}\mathfrak{D}_{x_3} & -\frac{1}{\varepsilon^2}\Delta_h \bar{C}^2 \bar{\Theta}^{-1} \\ -\frac{1}{\varepsilon^2}\mathfrak{D}_{x_3}\bar{\Theta} & -\frac{1}{\varepsilon^2}\nabla_h \cdot ((\mathbb{1}_{3N} \otimes \bar{\Theta})\nabla_h \bar{C}^2 \bar{\Theta}^{-1}) \end{bmatrix}. \tag{30b}$$

We have denoted by Δ_h, ∇_h and $\nabla_h \cdot$ the discrete Laplace, gradient and divergence operators, that arise from the central differences operators $\mathfrak{D}_{x_s}$, respectively. After computing the potential temperature and density we can evaluate the momentum explicitly

$$\mathbf{Q}_j^{n+1} = \hat{\mathbf{Q}}_j - \frac{\Delta t}{\varepsilon^2}\mathfrak{D}_{x_j}\bar{C}^2\bar{\Theta}^{-1}(\boldsymbol{\rho\theta})'^{n+1}, \quad j = 1, 2, \tag{31a}$$

$$\mathbf{Q}_3^{n+1} = \hat{\mathbf{Q}}_3 - \frac{\Delta t}{\varepsilon^2}\mathfrak{D}_{x_3}\bar{C}^2\bar{\Theta}^{-1}(\boldsymbol{\rho\theta})'^{n+1} - \frac{\Delta t}{\varepsilon^2}\boldsymbol{\rho}'^{n+1}. \tag{31b}$$

In what follows we will assume that $\bar{\theta} = \text{const}$. This allows us to simplify the discrete system (30) and eliminate the density from the potential temperature equation

$$\left[\mathbb{1} - \frac{\Delta t^2}{\varepsilon^2}E\right](\boldsymbol{\rho\theta})'^{n+1} = (\hat{\boldsymbol{\rho\theta}})' - \Delta t\bar{\Theta}\nabla_h \cdot \hat{\mathbf{Q}} - \frac{\Delta t^2}{\varepsilon^2}\mathfrak{D}_{x_3}(\widehat{(\boldsymbol{\rho\theta})}' - \bar{\Theta}\hat{\boldsymbol{\rho}}'), \tag{32}$$

where

$$E := \Delta_h \bar{C}^2 + \mathfrak{D}_{x_3}.$$

Finally, we have to solve only the elliptic equation for the discrete potential temperature $(\boldsymbol{\rho\theta})'^{n+1}$. This can be realized by any suitable linear solver; in the numerical experiments presented below we have applied the direct solver UMFPACK [16]. Having obtained the potential temperature at the new time step we can update the momentum by (31) and the density from the eliminated equation

$$\boldsymbol{\rho}'^{n+1} = \hat{\boldsymbol{\rho}}' + \bar{\Theta}^{-1}((\boldsymbol{\rho\theta})'^{n+1} - \widehat{(\boldsymbol{\rho\theta})}'). \tag{33}$$

In order to further analyse the structure of the resulting linear system (32) we assume for simplicity that periodic boundary conditions are applied. Then the operator $-\Delta_h$ is positive semi-definite and $\mathfrak{D}_{x_3}$ is anti-symmetric. Consequently, the matrix $\left[\mathbb{1} - \frac{\Delta t^2}{\varepsilon^2}(\Delta_h \bar{C}^2 + \mathfrak{D}_{x_3})\right]$ is positive definite and non-singular. Thus, the matrix $\mathbb{1} - \frac{\Delta t^2}{\varepsilon^2}E$ is non-singular for any $\varepsilon > 0$. This leads us to the following lemma.

Lemma 4.1 *Let the background potential temperature $\bar{\theta} = \text{const}$. and the periodic boundary conditions be applied. Then the linear system (32) has a unique solution for any $\varepsilon > 0$.*

Lemma 4.2 *For any $\mathbf{x} \in \mathbb{R}^N$ it holds*

$$\mathfrak{D}_{x_3}\bar{C}^2\mathbf{x} = \bar{C}^2\mathfrak{D}_{x_3}\mathbf{x} + (1-\gamma)\mathfrak{M}_{x_3}\mathbf{x}, \tag{34}$$

where $\mathfrak{M}_{x_3}$ denotes the block matrix arising from the average operator $\mu_x f_i = 0.5(f_{i+1} + f_{i-1})$ in the x_3-direction.

Proof: Let us recall that the discrete product rule gives $\delta_x(fg)_i = \mu_x f_i \delta_x g_i + \delta_x f_i \mu_x g_i$, where i denotes an index of a mesh cell. Further we have for any $\mathbf{x} \in \mathbb{R}^N$

$$\mathfrak{D}_{x_3}\bar{C}^2\mathbf{x} = \mathfrak{M}_{x_3}\bar{C}^2\mathfrak{D}_{x_3}\mathbf{x} + (\bar{C}^2)_{x_3}\mathfrak{M}_{x_3}\mathbf{x},$$

where $(\bar{C}^2)_{x_3}$ denotes the diagonal matrix representing the function $\partial(\bar{c}^2)/\partial x_3$. We know due to Lemma 2.1 that $\bar{c}^2 = \gamma\bar{\theta} - (\gamma-1)x_3$. Thus, we have $(\bar{C}^2)_{x_3} = (1-\gamma)\mathbb{1}$ and $\mathfrak{M}_{x_3}\bar{C}^2 = \bar{C}^2$. □

Remark 4.3 *We will use the following properties*

1. $\mathfrak{D}_{x_i}, i = 1,2,3$ *and* $\mathfrak{M}_{x_3}$ *commute and can be diagonalised (since they are circulant matrices, cf. [15])*
2. $\mathfrak{D}_{x_i}$, $i = 1,2,3$, *are anti-symmetric*
3. $\mathfrak{M}_{x_3}$ *is symmetric*
4. $\mathfrak{D}_{x_i}, i = 1,2$ *and* $\bar{C}^2$ *commute (since* $\bar{c}^2$ *only depends on their vertical coordinate* x_3*).*

Lemma 4.4 *Under the assumptions of Lemma 4.1 we have* $Ker(E) = Ker(\nabla_h)$*, where* $Ker(E)$ *and* $Ker(\nabla_h)$ *denote nullspaces of* E *and* ∇_h *operators, respectively.*

Proof: First, we have for any $\mathbf{x} \in \mathbb{R}^N$ that $\mathbf{x}^T\mathfrak{D}_{x_3}^T\mathfrak{M}_{x_3}\mathbf{x} = 0$. Indeed, realizing that $\mathfrak{B} = \mathfrak{B}^T$ for any $\mathfrak{B} \in \mathbb{R}^{1\times 1}$ we get

$$\mathbf{x}^T\mathfrak{D}_{x_3}^T\mathfrak{M}_{x_3}\mathbf{x} = (\mathbf{x}^T\mathfrak{D}_{x_3}^T\mathfrak{M}_{x_3}\mathbf{x})^T = -\mathbf{x}^T\mathfrak{D}_{x_3}^T\mathfrak{M}_{x_3}\mathbf{x}. \tag{35}$$

Thus, applying the discrete product rule for $\mathfrak{D}_{x_3}\bar{C}^2\mathbf{x}$ we obtain

$$\mathbf{x}^T E\mathbf{x} = -\mathbf{x}^T\sum_{i=1}^{3}\mathfrak{D}_{x_i}^T\bar{C}^2\mathfrak{D}_{x_i}\mathbf{x} - \mathbf{x}^T\mathfrak{D}_{x_3}^T(1-\gamma)\mathfrak{M}_{x_3}\mathbf{x} = -\sum_{i=1}^{3}\|\bar{C}\mathfrak{D}_{x_i}\mathbf{x}\|_2^2. \tag{36}$$

This implies $Ker(E) \subset Ker(\nabla_h)$, since $\bar{C}^2$ is regular. Let $\nabla_h\mathbf{x} = 0$, i.e. $\mathfrak{D}_{x_i}\mathbf{x} = 0$, $i = 1,2,3$. Then, we have

$$E\mathbf{x} = \sum_{i=1}^{3}\mathfrak{D}_{x_i}\bar{C}^2\mathfrak{D}_{x_i}\mathbf{x} + \mathfrak{D}_{x_3}(1-\gamma)\mathfrak{M}_{x_3}\mathbf{x} + \mathfrak{D}_{x_3}\mathbf{x} = 0, \tag{37}$$

which leads us to $Ker(\nabla_h) \subset Ker(E)$. □

Analyzing the multiplicity of the zero eigenvalue of the matrix E we obtain the following interesting projection property.

Lemma 4.5 *Let the assumptions from Lemma 4.1 hold. Then the algebraic multiplicity of the eigenvalue zero of the matrix* E *equals its geometric multiplicity.*

Proof: We have to show that $E^2\mathbf{x} = 0$ implies $E\mathbf{x} = 0$. Due to Lemma 4.4 this statement is equivalent to: $\nabla_h E\mathbf{x} = 0$ implies $\nabla_h\mathbf{x} = 0$. Suppose $\nabla_h E\mathbf{x} = 0$. Then we have

$$0 = \mathbf{x}^T\mathfrak{D}_{x_j}^2\sum_{i=1}^{3}\mathfrak{D}_{x_i}^2\bar{C}^2\mathbf{x} + \mathbf{x}^T\mathfrak{D}_{x_j}^2\mathfrak{D}_{x_3}\mathbf{x} = \sum_{i=1}^{3}\mathbf{x}^T\mathfrak{D}_{x_j}^2\mathfrak{D}_{x_i}^2\bar{C}^2\mathbf{x} = \sum_{i=1}^{3}\|\bar{C}\mathfrak{D}_{x_j}\mathfrak{D}_{x_i}\|_2^2$$

for $j = 1,2$. Thus $\mathbf{x} \in Ker(\mathfrak{D}_{x_j}^2)$, $j = 1,2$. Analogously we have

$$\begin{aligned} 0 &= \mathbf{x}^T\mathfrak{D}_{x_3}^2\sum_{i=1}^{3}\mathfrak{D}_{x_i}^2\bar{C}^2\mathbf{x} + \mathbf{x}^T\mathfrak{D}_{x_3}^3\mathbf{x} = \sum_{i=1}^{3}\left(\mathbf{x}^T\mathfrak{D}_{x_3}\mathfrak{D}_{x_i}^2\bar{C}^2\mathfrak{D}_{x_3}\mathbf{x} + (1-\gamma)\mathbf{x}^T\mathfrak{D}_{x_3}\mathfrak{D}_{x_i}^2\mathbf{x}\right) \\ &= \sum_{i=1}^{3}\|\bar{C}\mathfrak{D}_{x_3}^2\|_2^2, \end{aligned}$$

which implies $\mathbf{x} \in Ker(\mathfrak{D}_{x_3}^2)$. Since the matrices $\mathfrak{D}_{x_i}$, $i = 1,2,3$, are diagonalisable, the nullspaces of $\mathfrak{D}_{x_i}^2$ and $\mathfrak{D}_{x_i}$ are identical. □

Lemma 4.6 *Let the assumptions from Lemma 4.1 hold. Then, we have the projection property*

$$\left(\mathbb{1} - \frac{\Delta t^2}{\varepsilon^2} E\right)^{-1} = \pi_{Ker(E)} + \mathcal{O}(\varepsilon^2), \tag{38}$$

where $\pi_{Ker(E)}$ is the projection onto $Ker(E)$ along $\mathcal{R}(E)$; $\mathcal{R}(E)$ denotes the range of the matrix E. Moreover, we also have that the limit of (38) as $\varepsilon \to 0$ is $\pi_{Ker(E)}$.

Proof: Let $R^{-1}ER$ be the Jordan normal form of the matrix E. Then, $R^{-1}(\mathbb{1} - \frac{\Delta t^2}{\varepsilon^2}E)R$ is the Jordan normal form of $(\mathbb{1} - \frac{\Delta t^2}{\varepsilon^2}E)$. Note, that the matrix R is independent of ε. Thus, it suffices to consider the Jordan blocks

$$J = \begin{pmatrix} \lambda & 1 & 0 & \cdots & 0 \\ 0 & \lambda & 1 & & \vdots \\ \vdots & \ddots & \ddots & \ddots & 0 \\ 0 & & 0 & \lambda & 1 \\ 0 & \cdots & \cdots & 0 & \lambda \end{pmatrix},$$

where $\lambda = 1 - (\Delta t/\varepsilon)^2\mu$, μ being an eigenvalue of E. Note that $\lambda \neq 0$, since $\mathbb{1} - \frac{\Delta t^2}{\varepsilon^2}E$ is non-singular, cf. Lemma 4.1. Hence, we can compute the inverse of J, cf. [24, Section 9.1.1],

$$J^{-1} = \begin{pmatrix} \lambda^{-1} & -\lambda^{-2} & \cdots & \cdots & (-1)^{n-1}\lambda^{-n} \\ 0 & \lambda^{-1} & -\lambda^{-2} & \cdots & (-1)^{n-2}\lambda^{-(n-1)} \\ \vdots & \ddots & \ddots & \ddots & \vdots \\ 0 & & 0 & \lambda^{-1} & -\lambda^{-2} \\ 0 & \cdots & \cdots & 0 & \lambda^{-1} \end{pmatrix}.$$

We have

$$\lambda^{-1} = \frac{\varepsilon^2}{\varepsilon^2 - \Delta t^2 \mu} = \begin{cases} 1, & \text{if } \mu = 0 \\ \mathcal{O}(\varepsilon^2), & \text{else.} \end{cases}$$

Consequently, $J^{-1} = \mathcal{O}(\varepsilon^2)$ for $\mu \neq 0$. Due to Lemma 4.5 the Jordan blocks corresponding to the eigenvalue zero are diagonal. Hence, $J^{-1} = \mathbb{1}$ for $\mu = 0$. □

Theorem 4.7 *Let the assumption of Lemma 4.1 hold and $\rho'^n, (\rho\theta)'^n = \mathcal{O}(\varepsilon^2)$. Then the numerical solution satisfies the following asymptotic preserving properties*

$$(\rho\theta)'^{n+1}, \rho'^{n+1}, \nabla_h \cdot \mathbf{Q}^{n+1} = \mathcal{O}(\varepsilon^2), \tag{39}$$

if a numerical flux for the explicit finite volume scheme obeys the following property:

$$\rho'^n, (\rho\theta)'^n = \mathcal{O}(\varepsilon^2) \;\Rightarrow\; \hat{\rho}', \widehat{(\rho\theta)}' = \mathcal{O}(\varepsilon^2). \tag{40}$$

Proof: First, we note that (36) implies $Ker(E^T) \subset Ker(\nabla_h) = Ker(E)$. Since the dimensions of the kernel of E and E^T are equal, we have $Ker(E^T) = Ker(E)$. Consequently $Ker(E)^\perp = \mathcal{R}(E)$ and the projection in (38) is the orthogonal projection on $Ker(E)$. Further,

$$\mathcal{R}(E) = Ker(E)^\perp = Ker(\nabla_h)^\perp = \mathcal{R}(\nabla_h^T) = \mathcal{R}(\nabla_h \cdot). \tag{41}$$

This yields $(\rho\theta)'^{n+1} = \pi_{Ker(E)}\widehat{(\rho\theta)}' + \mathcal{O}(\varepsilon^2) = \mathcal{O}(\varepsilon^2)$. From (33) we obtain

$$\rho'^{n+1} = \hat{\rho}' + \frac{(\rho\theta)'^{n+1} - \widehat{(\rho\theta)}'}{\bar{\theta}} = \mathcal{O}(\varepsilon^2). \tag{42}$$

From the continuity or the potential temperature equation we conclude, that $\nabla_h \cdot \mathbf{Q}^{n+1} = \mathcal{O}(\varepsilon^2)$.

□

Remark 4.8 *Let the initial data satisfy* $\rho'(0,\cdot) = \mathcal{O}(\varepsilon^2)$, $(\rho\theta)'(0,\cdot) = \mathcal{O}(\varepsilon^2)$. *Then one can apply a suitable explicit finite volume method to approximate the nonlinear subsystem (19), that will preserve this property, i.e. (40). For example, the Lax-Friedrichs method used below is one possible choice.*

We would like to point out that the divergence property of the momentum is controlled in our scheme only in the implicit step. For alternative approaches, where the divergence of momentum is either controlled by the extrapolation of the advective fluxes from the previous time step or by the MAC-type projection, we refer a reader to, e.g., [49].

Corollary 4.9 *Let the initial data of (1) be well-prepared, i.e.*

$$\rho(0,\cdot) = \bar{\rho} + \varepsilon^2 \rho^{(2)}(0,\cdot), \quad \theta(0,\cdot) = \bar{\theta} + \varepsilon^2 \theta^{(2)}(0,\cdot),\ \bar{\theta} = const.,$$

Then in the limit as $\varepsilon \to 0$ *the IMEX FV scheme yields a consistent approximation of the limiting anelastic equations*

$$\begin{aligned} &\nabla \cdot (\mathbf{q}^{(0)}) = 0, \quad \mathbf{q}^{(0)} \equiv \rho^{(0)}\mathbf{u}^{(0)} \\ &\partial_t(\rho^{(0)}\mathbf{u}^{(0)}) + \nabla \cdot \left(\rho^{(0)}\mathbf{u}^{(0)} \otimes \mathbf{u}^{(0)}\right) + \nabla \Pi = -\rho^{(2)}\mathbf{e}_3, \\ &\partial_t \theta^{(2)} + \mathbf{u}^{(0)} \cdot \nabla \theta^{(2)} = 0, \end{aligned} \tag{43}$$

where $\rho^{(0)} = \bar{\rho}$, $\theta^{(0)} = \bar{\theta}$, $(\rho\theta)^{(2)} = \lim_{\varepsilon\to 0} \frac{(\rho\theta)'}{\varepsilon^2}$, $\rho^{(2)} = \lim_{\varepsilon\to 0} \frac{\rho'}{\varepsilon^2}$, $\theta^{(2)} = ((\rho\theta)^{(2)} - \rho^{(2)}\bar{\theta})/(\bar{\rho} + \rho^{(2)})$. *Further,* Π *is the pressure, the presence of which is enforced by the divergence freedom of the momentum, i.e.* Π *acts as the corresponding Lagrange multiplier.*

Proof: follows from the fact that our IMEX FV scheme gives an asymptotic consistent approximation of the Euler equations (1) and from the formal asymptotic analysis; see also a recent result of Feireisl et al. [19], where the convergence of the solution of (1) to a smooth solution of the incompressible limit is rigorously proven. □

5 Asymptotic preserving properties: stability

The aim of this section is to discuss asymptotic stability of our IMEX schemes. We will again concentrate on the first order IMEX FV method (20), (23), (24), (27). Applying the operator splitting approach we analyse firstly asymptotic stability of the linear subsystem, that is approximated implicitly in time and by the central differences in space.

Let us denote by $\Omega \subset \mathbb{R}^3$ a computational domain and let $\mathbf{w}_h^{n+1} = \left(\rho_h'^{n+1}, \mathbf{q}_h^{n+1}, (\rho\theta)_h'^{n+1}\right)$, $\hat{\mathbf{w}}_h = \left(\hat{\rho}_h', \hat{\mathbf{q}}_h, (\widehat{\rho\theta})_h'\right)$ be the discrete solutions of the linear subsystem (18) and the nonlinear subsystem (19), respectively. Note that $\mathbf{w}_h^{n+1} : \Omega \to \mathbb{R}^5$ is a piecewise constant function in space, such that $\mathbf{w}_h^{n+1}\Big|_{\Omega_{i,j,m}} \equiv \mathbf{w}_{i,j,m}^{n+1}$ for all mesh cells $\Omega_{i,j,m}$. Analogous notation holds for $\hat{\mathbf{w}}_h$. We concentrate here on the linear subsystem (18) without gravitation, the proof of asymptotic stability for the Euler equation with the gravity term is more delicate and will be considered in our forthcoming paper. Our numerical scheme for (18) can be reformulated equivalently in the

following way

$$\begin{aligned}
&\frac{(\rho')_h^{n+1} - (\hat{\rho'})_h}{\Delta t} + \nabla_h \cdot \mathbf{q}_h^{n+1} = 0 \\
&\frac{\mathbf{q}_h^{n+1} - \hat{\mathbf{q}}_h}{\Delta t} + \frac{1}{\varepsilon^2 \bar{\theta}} \nabla_h (\bar{c}_h^2 (\rho\theta')_h^{n+1} = 0 \\
&\frac{((\rho\theta')_h^{n+1} - ((\widehat{\rho\theta})')_h}{\Delta t} + \nabla_h \cdot (\mathbf{q}_h^{n+1} \bar{\theta}) = 0,
\end{aligned} \tag{44}$$

where ∇_h and $\nabla_h \cdot$ denotes now the finite difference operators for the discrete gradient and discrete divergence arising from the central differences $\delta_{x_s}/(2\Delta x_s)$, $s = 1, 2, 3$. We will denote by $\|\mathbf{w}_h\|$ the discrete L^2-norm, i.e. $\|\mathbf{w}_h\|^2 = \int_\Omega (\mathbf{w}_h)^2 dxdydz = \sum_{i,j,m} |\Omega_{i,j,m}| (\mathbf{w}_{i,j,m})^2$. Here the summation is done over all indices i, j, m, such that a mesh cell $\Omega_{i,j,m} \subseteq \Omega$ and $|\Omega_{i,j,m}|$ denotes the volume of the corresponding mesh cell.

In what follows we assume that either periodic or no-flux boundary conditions are prescribed. In the latter case we set $\mathbf{u} \cdot \mathbf{n} = 0$ and enforce additionally the numerical boundary conditions $\nabla_h \bar{c}_h^2 (\rho\theta)'_h \cdot \mathbf{n} = 0 = \nabla_h \rho'_h \cdot \mathbf{n}$ for ghost cells. Thus, we extrapolate the linearized pressure and the density in the normal direction. These types of boundary conditions have been also used in our numerical experiments presented below. Analogously as in the previous section we do not consider in our stability analysis arbitrary background stratifications of potential temperature, but confine ourselves to the case of $\bar{\theta} = const$.

Theorem 5.1 (Asymptotic stability for the linear subsystem)
Let us assume that $\bar{\theta} = const.$ and periodic or no-flux boundary conditions are used. Then the implicit finite difference approximation of the linear subsystem (15) is asymptotically stable, i.e. we have for any $0 < \varepsilon \ll 1$

$$\left\| \frac{\bar{c}_h}{\varepsilon \bar{\theta}} (\rho\theta)'^{n+1}_h \right\| + \|\mathbf{q}_h^{n+1}\| + \|(\rho\theta')_h^{n+1}\| \leq \left\| \frac{\bar{c}_h}{\varepsilon \bar{\theta}} (\widehat{\rho\theta})'_h \right\| + \|\hat{\mathbf{q}}_h\| + \|\widehat{\rho\theta'}_h\|. \tag{45}$$

Proof: By substituting $(15)_2$ into $(15)_3$ we get

$$(\rho\theta)'^{n+1}_h - \left(\frac{\Delta t}{\varepsilon}\right)^2 \nabla_h \cdot \left(\nabla_h (\bar{c}_h^2 (\rho\theta)'^{n+1}_h) \right) = (\widehat{\rho\theta})'_h - \Delta t \nabla_h \cdot (\bar{\theta} \hat{\mathbf{q}}_h). \tag{46}$$

Analogously, we also have

$$(\rho')_h^{n+1} - \left(\frac{\Delta t}{\varepsilon}\right)^2 \nabla_h \cdot \left(\nabla_h \left(\frac{\bar{c}_h^2}{\bar{\theta}} (\rho\theta)'^{n+1}_h \right) \right) = (\hat{\rho'})_h - \Delta t \nabla_h \cdot (\hat{\mathbf{q}}_h). \tag{47}$$

Now we multiply the equation (46) by $\frac{\bar{c}_h^2}{\bar{\theta}^2 \varepsilon^2} (\rho\theta)'^{n+1}_h$ and $(15)_2$ by $\hat{\mathbf{q}}_h$, integrating over Ω yields

$$\frac{1}{2}\|\mathbf{q}_h^{n+1}\|^2 - \frac{1}{2}\|\hat{\mathbf{q}}_h\|^2 - \frac{1}{2}\|\mathbf{q}_h^{n+1} - \hat{\mathbf{q}}_h\|^2 + \Delta t \frac{1}{\varepsilon^2 \bar{\theta}} \int_\Omega \nabla_h \left(\bar{c}_h^2 (\rho\theta)'^{n+1}_h \right) \hat{\mathbf{q}}_h = 0 \tag{48}$$

$$\begin{aligned}
&\frac{1}{2}\left\| \frac{\bar{c}_h}{\varepsilon \bar{\theta}} (\rho\theta)'^{n+1}_h \right\|^2 - \frac{1}{2}\left\| \frac{\bar{c}_h}{\varepsilon \bar{\theta}} (\widehat{\rho\theta})'_h \right\|^2 + \frac{1}{2}\left\| \frac{\bar{c}_h}{\varepsilon \bar{\theta}} (\rho\theta)'^{n+1}_h - \frac{\bar{c}_h}{\varepsilon \bar{\theta}} (\widehat{\rho\theta})'_h \right\|^2 \\
&+ \Delta t \int_\Omega \frac{\bar{c}_h^2}{\varepsilon^2 \bar{\theta}} (\rho\theta)'^{n+1}_h \nabla_h \cdot \hat{\mathbf{q}}_h + \left(\frac{\Delta t}{\varepsilon}\right)^2 \left\| \nabla_h \left(\frac{\bar{c}_h^2}{\varepsilon \bar{\theta}} (\rho\theta)'^{n+1}_h \right) \right\|^2 = 0,
\end{aligned} \tag{49}$$

where we have used the discrete integration by parts and periodic or no-flux boundary conditions. Summing (48) and (49) leads to

$$\frac{1}{2}\|\mathbf{q}_h^{n+1}\|^2-\frac{1}{2}\|\hat{\mathbf{q}}_h\|^2-\frac{1}{2}\|\mathbf{q}_h^{n+1}-\hat{\mathbf{q}}_h\|^2+\frac{1}{2}\Big\|\frac{\bar{c}_h}{\varepsilon\bar{\theta}}(\rho\theta)_h'^{n+1}\Big\|^2-\frac{1}{2}\Big\|\frac{\bar{c}_h}{\varepsilon\bar{\theta}}(\widehat{\rho\theta})_h'\Big\|^2$$
$$+\frac{1}{2}\Big\|\frac{\bar{c}_h}{\varepsilon\bar{\theta}}(\rho\theta)_h'^{n+1}-\frac{\bar{c}_h}{\varepsilon\bar{\theta}}(\widehat{\rho\theta})_h'\Big\|^2+\left(\frac{\Delta t}{\varepsilon}\right)^2\Big\|\nabla_h\left(\frac{\bar{c}_h^2}{\varepsilon\bar{\theta}}(\rho\theta)_h'^{n+1}\right)\Big\|^2=0. \tag{50}$$

From the momentum equation $(15)_2$ we obtain

$$\frac{1}{2}\|\mathbf{q}_h^{n+1}-\hat{\mathbf{q}}_h\|^2=\frac{1}{2}\left(\frac{\Delta t}{\varepsilon}\right)^2\Big\|\nabla_h\left(\frac{\bar{c}_h}{\varepsilon\bar{\theta}}(\rho\theta)_h'^{n+1}\right)\Big\|^2. \tag{51}$$

Substituting (51) into (50) yields

$$\frac{1}{2}\|\mathbf{q}_h^{n+1}\|^2-\frac{1}{2}\|\hat{\mathbf{q}}_h\|^2+\frac{1}{2}\Big\|\frac{\bar{c}_h}{\varepsilon\bar{\theta}}(\rho\theta)_h'^{n+1}\Big\|^2-\frac{1}{2}\Big\|\frac{\bar{c}_h}{\varepsilon\bar{\theta}}(\widehat{\rho\theta})_h'\Big\|^2$$
$$+\frac{1}{2}\Big\|\frac{\bar{c}_h}{\varepsilon\bar{\theta}}(\rho\theta)_h'^{n+1}-\frac{\bar{c}_h}{\varepsilon\bar{\theta}}(\widehat{\rho\theta})_h'\Big\|^2+\frac{1}{2}\left(\frac{\Delta t}{\varepsilon}\right)^2\Big\|\nabla_h\left(\frac{\bar{c}_h^2}{\varepsilon\bar{\theta}}(\rho\theta)_h'^{n+1}\right)\Big\|^2=0 \tag{52}$$

and we obtain

$$\|\mathbf{q}_h^{n+1}\|^2+\Big\|\frac{\bar{c}_h}{\varepsilon\bar{\theta}}(\rho\theta)_h'^{n+1}\Big\|^2+\Big\|\frac{\bar{c}_h}{\varepsilon\bar{\theta}}(\rho\theta)_h'^{n+1}-\frac{\bar{c}_h}{\varepsilon\bar{\theta}}(\widehat{\rho\theta})_h'\Big\|^2+\left(\frac{\Delta t}{\varepsilon}\right)^2\Big\|\nabla_h\left(\frac{\bar{c}_h^2}{\varepsilon\bar{\theta}}(\rho\theta)_h'^{n+1}\right)\Big\|^2$$
$$=\|\hat{\mathbf{q}}_h\|^2+\Big\|\frac{\bar{c}_h}{\varepsilon\bar{\theta}}(\widehat{\rho\theta})_h'\Big\|^2.$$

This leads to the desired stability estimate

$$\|\mathbf{q}_h^{n+1}\|^2+\Big\|\frac{\bar{c}_h}{\varepsilon\bar{\theta}}(\rho\theta)_h'^{n+1}\Big\|^2\leq\ \|\hat{\mathbf{q}}_h\|^2+\Big\|\frac{\bar{c}_h}{\varepsilon\bar{\theta}}(\widehat{\rho\theta})_h'\Big\|^2. \tag{53}$$

We also note that the asymptotic consistency analysis presented in the previous section shows that $\mathbf{q}_h^{n+1}=\mathcal{O}(1)$, while $(\rho\theta)_h'^{n+1}=\mathcal{O}(\varepsilon^2)=(\rho')_h^{n+1}$. Combining this fact with (53), which is uniform in $\varepsilon>0$, yields also

$$\|\mathbf{q}_h^{n+1}\|\leq\|\hat{\mathbf{q}}_h\|,\qquad\Big\|\frac{\bar{c}_h}{\varepsilon\bar{\theta}}(\rho\theta)_h'^{n+1}\Big\|\leq\Big\|\frac{\bar{c}_h}{\varepsilon\bar{\theta}}(\widehat{\rho\theta})_h'\Big\|. \tag{54}$$

Multiplying (47) by $\bar{\theta}$ we obtain

$$(\rho\theta')_h^{n+1}\equiv(\rho\theta)_h'^{n+1}-\bar{\theta}(\rho')_h^{n+1}=(\widehat{\rho\theta})_h'-\bar{\theta}\hat{\rho}'_h\equiv\widehat{\rho\theta}'_h \tag{55}$$

and consequently $\|(\rho\theta')_h^{n+1}\|=\|\widehat{\rho\theta}'_h\|$, which concludes the proof. □

Remark 5.2 *Applying the triangular inequality to (55) leads to the boundedness of the density as well* $\|(\rho')_h^{n+1}\|\leq\|\hat{\rho}'_h\|+\frac{1}{\bar{\theta}}\|(\hat{\rho\theta})'_h\|+\frac{1}{\bar{\theta}}\|(\rho\theta)_h'^{n+1}\|$. *Combining it with (53) we obtain the following stability estimate*

$$\|\mathbf{q}_h^{n+1}\|+\Big\|\frac{\bar{c}_h}{\varepsilon\bar{\theta}}(\rho\theta)_h'^{n+1}\Big\|+\Big\|\frac{\bar{c}_h}{\varepsilon}(\rho')_h^{n+1}\Big\|\leq\|\hat{\mathbf{q}}_h\|+3\Big\|\frac{\bar{c}_h}{\varepsilon\bar{\theta}}(\widehat{\rho\theta})_h'\Big\|+\Big\|\frac{\bar{c}_h}{\varepsilon}\hat{\rho}'_h\Big\|. \tag{56}$$

Next, we will study stability of the nonlinear subsystem that is discretized explicitly by, e.g., the Lax-Friedrichs scheme.

$$\begin{aligned}
\hat{\rho}'_{ijm} &= \frac{1}{3}\left(\mu_{x_1}\rho' + \mu_{x_2}\rho' + \mu_{x_3}\rho'\right)^n_{ijm} \\
\hat{\mathbf{q}}_{ijm} &= \frac{1}{3}\left(\mu_{x_1}\mathbf{q} + \mu_{x_2}\mathbf{q} + \mu_{x_3}\mathbf{q}\right)^n_{ijm} - \Delta t \sum_{s=1}^{3} \frac{1}{2\Delta x_s}\delta_{x_s}(\mathbf{q}\mathbf{u}_s)^n_{ijm} \\
\widehat{(\rho\theta)}'_{ijm} &= \frac{1}{3}\left(\mu_{x_1}(\rho\theta)' + \mu_{x_2}(\rho\theta)' + \mu_{x_3}(\rho\theta)'\right)^n_{ijm} - \Delta t \sum_{s=1}^{3} \frac{1}{2\Delta x_s}\delta_{x_s}(\rho\theta'\mathbf{u}_s)^n_{ijm}
\end{aligned} \tag{57}$$

In what follows, we will derive the uniform L^1-stability estimates with respect to $\varepsilon > 0$. To this end let us denote by $\|\cdot\|$ the discrete L^1-norm. Using the triangular inequality, no-flux or periodic boundary conditions we obtain

$$\begin{aligned}
\|\hat{\rho}_h\| \equiv \sum_{i,j,m} |\Omega_{ijm}||\hat{\rho}'_{ijm}| \leq \frac{1}{6}\sum_{i,j,m} |\Omega_{ijm}| \Big(&|\rho'^n_{i+1,j,m}| + |\rho'^n_{i-1,j,m}| + |\rho'^n_{i,j+1,m}| + |\rho'^n_{i,j-1,m}| \\
+|\rho'^n_{i,j,m+1}| + |\rho'^n_{i,j,m-1}|\Big) \leq \sum_{i,j,m} |\Omega_{ijm}||\rho'^n_{ijm}| \equiv \|\rho'^n_h\|.
\end{aligned} \tag{58}$$

Applying the CFL stability condition and the periodic or no-flux boundary conditions the momentum equation $(57)_2$ yields

$$\begin{aligned}
&\|\hat{\mathbf{q}}_h\| \equiv \sum_{i,j,m} |\Omega_{ijm}||\hat{\mathbf{q}}_{ijm}| \leq \\
&\frac{1}{2}\sum_{i,j,m} |\Omega_{ijm}|\Big|\left(\frac{1}{3} - \frac{\Delta t}{\Delta x_1}(\mathbf{u}^n_1)_{i+1,j,m}\right)\mathbf{q}^n_{i+1,j,m}\Big| + \Big|\left(\frac{1}{3} + \frac{\Delta t}{\Delta x_1}(\mathbf{u}^n_1)_{i-1,j,m}\right)\mathbf{q}^n_{i-1,j,m}\Big| \\
&+\frac{1}{2}\sum_{i,j,m} |\Omega_{ijm}|\Big|\left(\frac{1}{3} - \frac{\Delta t}{\Delta x_2}(\mathbf{u}^n_2)_{i,j+1,m}\right)\mathbf{q}^n_{i,j+1,m}\Big| + \Big|\left(\frac{1}{3} + \frac{\Delta t}{\Delta x_2}(\mathbf{u}^n_2)_{i,j-1,m}\right)\mathbf{q}^n_{i,j-1,m}\Big| \\
&+\frac{1}{2}\sum_{i,j,m} |\Omega_{ijm}|\Big|\left(\frac{1}{3} - \frac{\Delta t}{\Delta x_3}(\mathbf{u}^n_3)_{i,j,m+1}\right)\mathbf{q}^n_{i,j,m+1}\Big| + \Big|\left(\frac{1}{3} + \frac{\Delta t}{\Delta x_3}(\mathbf{u}^n_3)_{i,j,m-1}\right)\mathbf{q}^n_{i,j,m-1}\Big| \\
&= \frac{1}{2}\sum_{i,j,m} |\Omega_{ijm}| \sum_{s=1,2,3}\left[\left(\frac{1}{3} - \frac{\Delta t}{\Delta x_s}(\mathbf{u}^n_s)_{i,j,m}\right) + \left(\frac{1}{3} + \frac{\Delta t}{\Delta x_s}(\mathbf{u}^n_s)_{i,j,m}\right)\right]|\mathbf{q}^n_{ijm}| \leq \|\mathbf{q}^n_h\|.
\end{aligned} \tag{59}$$

We would like to point out that due to the dimensional splitting arguments we have used here a slightly stronger CFL_u stability condition than (25), namely we enforce that

$$\max_{s=1,2,3} \frac{|\mathbf{u}_s|\Delta t}{\Delta x_s} \leq 1/3. \tag{60}$$

Finally, multiplying $(57)_1$ by $\bar{\theta}$ and subtracting it from $(57)_3$ we obtain the discrete evolution for $(\rho\theta')_h$, which is analogous to the discrete equation $(57)_2$ for $\mathbf{q}_h$. Repeating the same arguments as above we obtain $\|\widehat{\rho\theta'}_h\| \leq \|(\rho\theta')^n_h\|$. Consequently, we have proven the following stability result.

Theorem 5.3 (Asymptotic stability for the nonlinear subsystem)
Let $\bar{\theta} = const.$ and the periodic or no-flux boundary conditions are used. Let the CFL_u stability condition (60) holds. Then the explicit approximation of the nonlinear subsystem by the Lax-Friedrichs scheme is asymptotically stable, i.e. we have for any $\varepsilon > 0$

$$\|\hat{\rho}'_h\| + \|\hat{\mathbf{q}}_h\| + \|\widehat{\rho\theta'}_h\| \leq \|\rho'^n_h\| + \|\mathbf{q}^n_h\| + \|(\rho\theta')^n_h\|. \tag{61}$$

Combing the results from Theorems 5.1, 5.3 and using the interpolation between the discrete L^1 and L^2-norm, cf. [14], we finally obtain stability of our IMEX FV scheme that holds uniformly with respect to $0 < \varepsilon \ll 1$. Note that our stability result holds in both L^1 and L^2-norms and for an arbitrary but fixed mesh and final time $T > 0$.

Theorem 5.4 (Asymptotic stability of the IMEX FV scheme)
Let $\bar{\theta} = const.$ and the periodic or no-flux boundary conditions are used. We assume that the CFL_u stability condition (60) holds. Then the IMEX FV scheme (20), (23), (24), (27) for the Euler equations is asymptotically stable, i.e. we have for any $0 < \varepsilon \ll 1$

$$\left\|\frac{\bar{c}_h}{\varepsilon\bar{\theta}}(\rho\theta)_h'^n\right\|+\|\mathbf{q}_h^n\|+\|(\rho\theta')_h^n\|+\left\|\frac{\bar{c}_h}{\varepsilon}(\rho')_h^n\right\| \leq c(\Delta x, T)\left(\left\|\frac{\bar{c}_h}{\varepsilon\bar{\theta}}(\rho\theta)_h'^0\right\| + \|\mathbf{q}_h^0\| + \|(\rho\theta')_h^0\| + \left\|\frac{\bar{c}_h}{\varepsilon}(\rho')_h^0\right\|\right),$$

where $(\rho_h'^0, \mathbf{q}_h^0, (\rho\theta)_h'^0)^T$ denotes the discrete initial data and the constant $c(\Delta x, T)$ depends on a mesh parameter $\Delta x \equiv \max_{s=1,2,3}(\Delta x_s)$, a final time $T > 0$ and a lower and upper bound of the background sound speed $\bar{c}$.

Remark 5.5 *(**Well-balanced property**) We note that our IMEX FV scheme is well-balanced by the construction. If we start with the numerical solution being in the hydrostatic equilibrium, i.e. $\mathbf{w}^n = \mathbf{0}$, then a new numerical solution will fulfill the same condition, $\mathbf{w}^{n+1} = \mathbf{0}$. Indeed, it is easy to verify that the nonlinear fluxes $\mathcal{H}_N(\mathbf{w}^n)$, cf. (24), vanish since $\mathbf{w}^n = \mathbf{0}$. Thus, the right-hand side of the linear system (18) is a zero vector. Since the matrix M in (18) is non-singular, the resulting solution $\mathbf{w}^{n+1} = \mathbf{0}$. Thus, the hydrostatic equilibrium is preserved. Consequently, the IMEX FV is well-balanced in the sense that it preserves the hydrostatic equilibrium state, which we have started from.*

6 Numerical experiments

In this section we present numerical results that demonstrate asymptotic preserving properties analysed above. In what follows we will use the acronyms

- EXP-RK2 for the explicit second order Runge-Kutta time discretisation and the finite volume method with the Rusanov flux for spatial discretization.
- IMEX-ARS2, cf. [2, 7], for the IMEX scheme with the ARS222 time discretisation, the finite volume method with the central differences for spatial discretization of the linear terms and the Rusanov flux for the nonlinear terms. Note that the scheme is based on the elliptic subsystem (32) instead of (18).
- IMEX-BDF2, cf. [3, 7], for the second order BDF2 scheme for time discretisation, the finite volume schemes with the central differences for spatial discretization of the linear terms and the Rusanov flux for the nonlinear terms. The scheme solves numerically the elliptic subsystem (32).

We apply the MUSCL approach for the nonlinear terms to obtain second order spatial discretisation. In what follows we analyse experimentally stability and convergence order of the above second order FV schemes. Test 1 and Test 3 in three space dimensions clearly shows the uniform stability as well as uniform second order convergence with respect to the singular parameter ε. This is due to the fact that the gravity/acoustic waves are not present in this experiment. In the consequent tests we have both the advective transport as well as the gravity/acoustic waves.

Although we still have uniform stability, we will not be able to obtain the second order convergence uniformly with respect to ε unless our discretisation parameter Δx is sufficiently small to resolve the fast waves. This fact has been pointed out by Jin [28]: AP schemes are convergent uniformly with ε. If ε scales are resolved by discretization parameters Δx, Δt of a particular scheme we get a good approximation of the limiting model, otherwise if ε is not resolved by discretization parameters a good approximation of the macroscopic model is obtained, see, e.g., [27], where this fact is confirmed also by theoretical analysis.

6.1 Test 1: Traveling Vortex

Inspired by the exact solution of the 2D shallow water equations in [48] we adopt the traveling vortex test to the Euler equations. To this end we set $p_0 = c_p = 2, c_v = 1$, $\theta = \bar{\theta} = 1$ and omit the gravity source term. Consequently, $R = 1$, $\gamma = 2$ and $p = \frac{1}{2}\rho^2$. Then, the Euler equations (1) are analogous to the shallow water equations with a constant bottom topography. The acoustic/advection splitting yields for the pressure term $p = p'_L + p'_{NL}$, $\quad p'_L = \bar{\rho}\rho'$, $\quad p'_{NL} = \frac{1}{2}\rho'^2$ and coincides with the splitting in the shallow water equations [8, 7]. The initial data read

$$\begin{aligned}
\rho(\mathbf{x},0) &= 110 + \left(\frac{\Gamma\eta}{\omega}\right)^2 (k(\omega r) - k(\pi))\chi_{\omega r \le \pi} \\
u(\mathbf{x},0) &= 0.6 + \Gamma(1+\cos(\omega r))(0.5 - x_2)\chi_{\omega r \le \pi} \\
v(\mathbf{x},0) &= \Gamma(1+\cos(\omega r))(x_1 - 0.5)\chi_{\omega r \le \pi}, \\
\theta(\mathbf{x},0) &= \bar{\theta} = 1,
\end{aligned} \tag{62}$$

where $r = \|\mathbf{x} - (0.5, 0.5)\|_2$, $\Gamma = 1.5$, $\omega = 4\pi$, $k(r) = 2\cos(r) + 2r\sin(r) + \frac{\cos(2r)}{8} + \frac{r}{4}\sin(2r) + 0.75r^2$. Here Γ is the so-called vortex intensity parameter, r_c the distance from the vortex core, and ω an angular wave frequency that specifies the vortex width. Let us point out that the underlying equilibrium is constant due to the absence of gravity effects. More precisely, $\bar{\rho} = \overline{\rho\theta} = 110$. For the corresponding non-dimensional equation we have

$$\varepsilon = M = \frac{u_{ref}}{\sqrt{\rho_{ref}}} = \frac{0.6\eta}{\sqrt{110}} \tag{63}$$

and the Mach number can be controlled by adjusting the value of η in (63).

The computational domain is set to $\Omega = [0,1] \times [0,1]$ and the periodic boundary conditions are used. The initial data are plotted in Figure 1. A rotating vortex, which is initially centered at $(0.5, 0.5)$, is transported to the right with the velocity 0.6. Thus, the exact solution reads $\mathbf{w}(\mathbf{x}, t) = \mathbf{w}(\mathbf{x} - 0.6t, 0)$. The numerical results obtained by the IMEX-ARS2 scheme for $\varepsilon = 10^{-1}, 10^{-3}$ after one period, i.e. $T = 5/3$, are shown in Figures 2, 3. Tables 1, 2 show the L^1-errors and the experimental convergence rates (EOC) of the IMEX-ARS2 and IMEX-BDF2 schemes. We observe the second order convergence rates almost uniformly with respect to ε. Table 3 contains the convergence rates of the explicit EXP-RK2 scheme. For $\varepsilon = 0.1$ the results of the traveling vortex test are similar for the considered explicit and IMEX schemes. However, the explicit scheme gives worse results in the asymptotic region, e.g., for $\varepsilon = 10^{-3}$, cf. Figure 4 and Table 3.

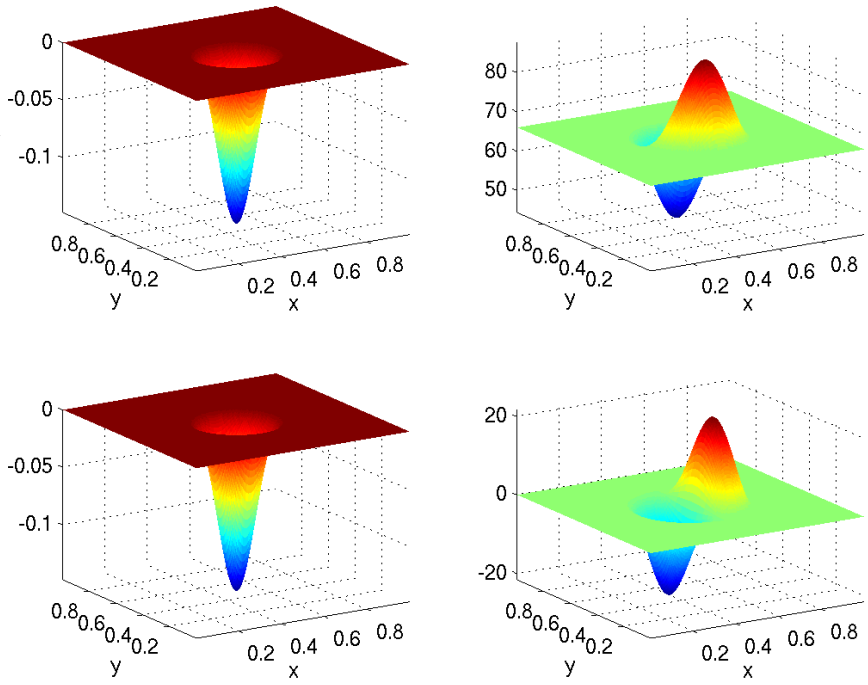

Figure 1: Traveling vortex test, $\varepsilon = 0.1$: initial data for $\mathbf{w}_1 = \rho'$ (left/upper), $\mathbf{w}_3 = (\rho\theta)'$ (left/lower), $\mathbf{w}_{2,1} = \rho u$ (right/upper), and $\mathbf{w}_{2,2} = \rho v$ (right/lower)

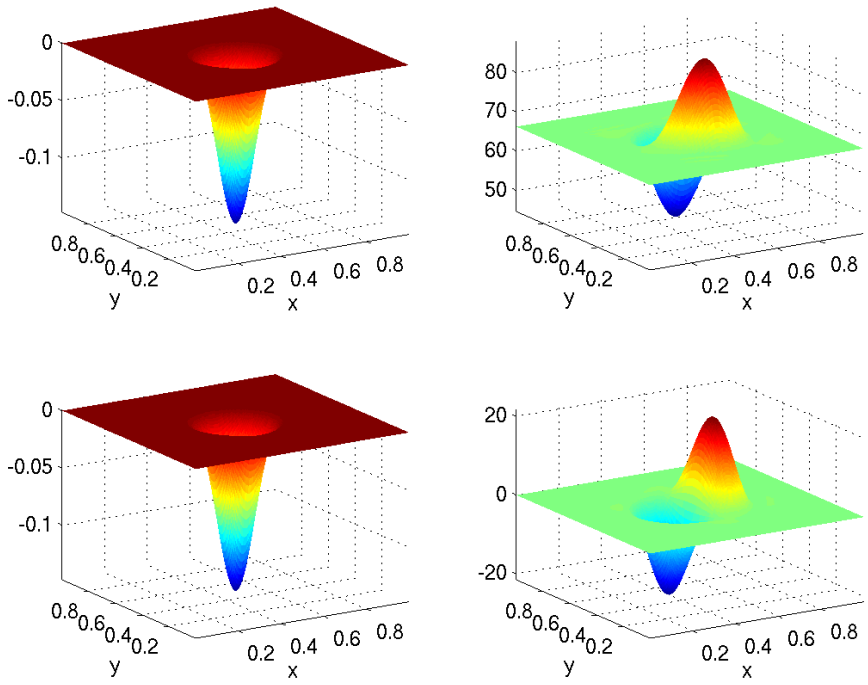

Figure 2: Traveling vortex test, $\varepsilon = 0.1$: numerical solution obtained by the IMEX-ARS2 scheme after one period ($T = 5/3$) for $\mathbf{w}_1 = \rho'$ (left/upper), $\mathbf{w}_3 = (\rho\theta)'$ (left/lower), $\mathbf{w}_{2,1} = \rho u$ (right/upper), and $\mathbf{w}_{2,2} = \rho v$ (right/lower). $\Delta x_1 = \Delta x_2 = 1/160$, $CFL_u = 0.45$, $CFL \approx 3.8$

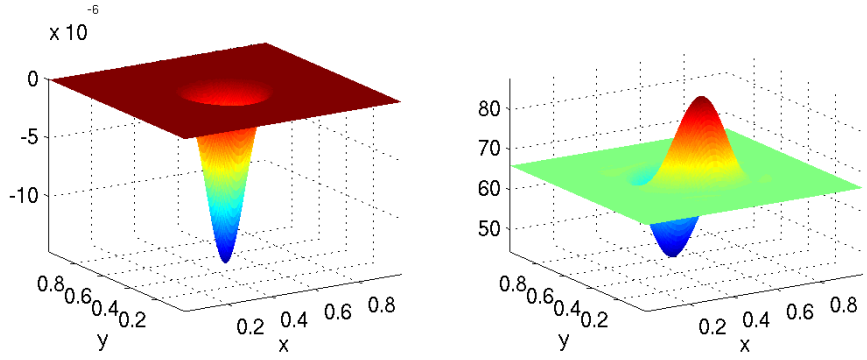

Figure 3: Traveling vortex test, $\varepsilon = 0.001$: numerical solution obtained by the IMEX-ARS2 scheme after one period ($T = 5/3$) for $\mathbf{w}_1 = \rho'$ (left) and $\mathbf{w}_{2,1} = \rho u$ (right). $\Delta x_1 = \Delta x_2 = 1/160$, $CFL_u = 0.45$, $CFL \approx 339$

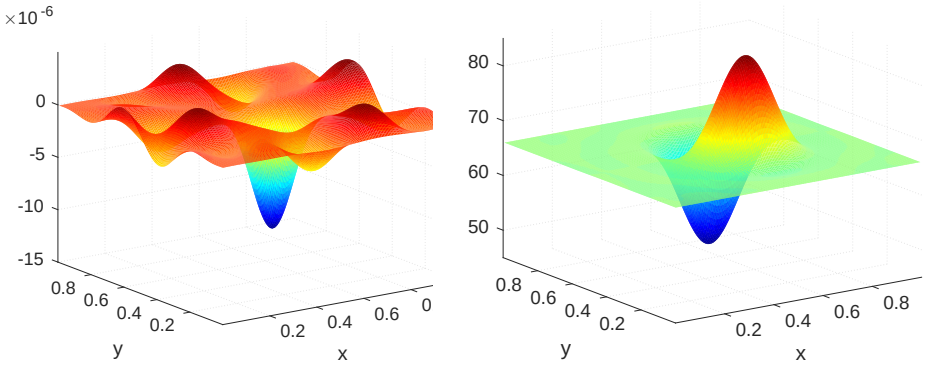

Figure 4: Traveling vortex test, $\varepsilon = 0.001$: numerical solution obtained by the EXP-RK2 scheme after one period ($T = 5/3$) for $\mathbf{w}_1 = \rho'$ (left) and $\mathbf{w}_{2,1} = \rho u$ (right). $\Delta x_1 = \Delta x_2 = 1/160$, $CFL = 0.45$

$\varepsilon = 10^{-1}$, $CFL \approx 3.8$

N	L^1-error ρ'	EOC ρ'	L^1-error m	EOC m	L^1-error n	EOC n	L^1-error $(\rho\theta)'$	EOC $(\rho\theta)'$
10	3.889e-02		4.826e-01		7.477e-01		3.889e-02	
20	9.341e-03	2.0576	1.247e-01	1.9527	2.764e-01	1.4358	9.341e-03	2.0576
40	3.209e-03	1.5414	3.699e-02	1.7528	7.098e-02	1.9613	3.209e-03	1.5414
80	7.935e-04	2.0160	1.027e-02	1.8483	1.827e-02	1.9578	7.935e-04	2.0160
160	1.908e-04	2.0559	2.893e-03	1.8283	4.894e-03	1.9003	1.908e-04	2.0559

$\varepsilon = 10^{-3}$, $CFL \approx 339$

N	L^1-error ρ'	EOC ρ'	L^1-error m	EOC m	L^1-error n	EOC n	L^1-error $(\rho\theta)'$	EOC $(\rho\theta)'$
10	7.554e-07		4.571e-01		7.742e-01		7.554e-07	
20	1.993e-07	1.9223	1.240e-01	1.8825	2.634e-01	1.5553	1.993e-07	1.9223
40	4.597e-08	2.1162	3.241e-02	1.9357	6.691e-02	1.9772	4.597e-08	2.1162
80	1.300e-08	1.8219	9.076e-03	1.8362	1.732e-02	1.9496	1.300e-08	1.8219
160	3.915e-09	1.7317	2.471e-03	1.8768	4.514e-03	1.9399	3.915e-09	1.7317

$\varepsilon = 10^{-5}$, $CFL \approx 33890$

N	L^1-error ρ'	EOC ρ'	L^1-error m	EOC m	L^1-error n	EOC n	L^1-error $(\rho\theta)'$	EOC $(\rho\theta)'$
10	7.576e-11		4.571e-01		7.742e-01		7.576e-11	
20	1.997e-11	1.9232	1.240e-01	1.8823	2.634e-01	1.5552	1.997e-11	1.9232
40	4.854e-12	2.0409	3.241e-02	1.9356	6.691e-02	1.9772	4.854e-12	2.0409
80	1.395e-12	1.7989	9.078e-03	1.8361	1.732e-02	1.9496	1.395e-12	1.7989
160	5.132e-13	1.4426	2.472e-03	1.8766	4.515e-03	1.9399	5.132e-13	1.4426

Table 1: Traveling vortex test: EOC for the IMEX-ARS2 scheme, $CFL_u = 0.45$, $T = 0.1$

$\varepsilon = 10^{-1}$, $CFL \approx 2.5$

N	L^1-error ρ'	EOC ρ'	L^1-error m	EOC m	L^1-error n	EOC n	L^1-error $(\rho\theta)'$	EOC $(\rho\theta)'$
10	3.233e-02		5.134e-01		7.980e-01		3.233e-02	
20	4.958e-03	2.7048	1.352e-01	1.9246	2.657e-01	1.5865	4.958e-03	2.7048
40	1.661e-03	1.5779	3.610e-02	1.9057	7.202e-02	1.8834	1.661e-03	1.5779
80	7.227e-04	1.2004	9.992e-03	1.8531	1.886e-02	1.9334	7.227e-04	1.2004
160	1.749e-04	2.0468	2.863e-03	1.8034	5.074e-03	1.8937	1.749e-04	2.0468

$\varepsilon = 10^{-3}$, $CFL \approx 226$

N	L^1-error ρ'	EOC ρ'	L^1-error m	EOC m	L^1-error n	EOC n	L^1-error $(\rho\theta)'$	EOC $(\rho\theta)'$
10	6.189e-07		4.963e-01		7.948e-01		6.189e-07	
20	1.777e-07	1.8005	1.363e-01	1.8641	2.751e-01	1.5308	1.777e-07	1.8005
40	4.900e-08	1.8585	3.453e-02	1.9809	7.034e-02	1.9674	4.900e-08	1.8585
80	1.270e-08	1.9478	9.496e-03	1.8626	1.845e-02	1.9304	1.270e-08	1.9478
160	3.299e-09	1.9449	2.562e-03	1.8899	4.835e-03	1.9323	3.299e-09	1.9449

$\varepsilon = 10^{-5}$, $CFL \approx 22590$

N	L^1-error ρ'	EOC ρ'	L^1-error m	EOC m	L^1-error n	EOC n	L^1-error $(\rho\theta)'$	EOC $(\rho\theta)'$
10	6.190e-11		4.963e-01		7.948e-01		6.190e-11	
20	1.777e-11	1.8007	1.363e-01	1.8641	2.751e-01	1.5308	1.777e-11	1.8007
40	4.900e-12	1.8585	3.453e-02	1.9809	7.034e-02	1.9674	4.900e-12	1.8585
80	1.270e-12	1.9481	9.496e-03	1.8627	1.845e-02	1.9305	1.270e-12	1.9481
160	3.299e-13	1.9446	2.562e-03	1.8899	4.835e-03	1.9324	3.298e-13	1.9448

Table 2: Traveling vortex test: EOC for the IMEX-BDF2 scheme, $CFL_u = 0.3$, $T = 0.1$

$\varepsilon = 10^{-1}$

N	L^1-error ρ'	EOC ρ'	L^1-error m	EOC m	L^1-error n	EOC n	L^1-error $(\rho\theta)'$	EOC $(\rho\theta)'$
10	8.441e-03		1.484e+00		1.297e+00		8.441e-03	
20	5.412e-03	0.6413	7.834e-01	0.9215	8.015e-01	0.6944	5.412e-03	0.6413
40	1.784e-03	1.6011	2.212e-01	1.8242	2.309e-01	1.7952	1.784e-03	1.6011
80	4.163e-04	2.0993	4.593e-02	2.2681	4.832e-02	2.2568	4.163e-04	2.0993
160	9.720e-05	2.0986	8.879e-03	2.3709	9.467e-03	2.3516	9.720e-05	2.0986

$\varepsilon = 10^{-3}$

N	L^1-error ρ'	EOC ρ'	L^1-error m	EOC m	L^1-error n	EOC n	L^1-error $(\rho\theta)'$	EOC $(\rho\theta)'$
10	7.509e-07		1.349e+00		1.221e+00		7.509e-07	
20	7.814e-07	-0.0575	1.472e+00	-0.1266	1.464e+00	-0.2618	7.814e-07	-0.0575
40	8.515e-07	-0.1239	1.731e+00	-0.2334	1.725e+00	-0.2367	8.515e-07	-0.1239
80	8.491e-07	0.0041	1.054e+00	0.7160	1.053e+00	0.7117	8.491e-07	0.0041
160	7.176e-07	0.2427	3.258e-01	1.6935	3.258e-01	1.6928	7.176e-07	0.2427

$\varepsilon = 10^{-5}$

N	L^1-error ρ'	EOC ρ'	L^1-error m	EOC m	L^1-error n	EOC n	L^1-error $(\rho\theta)'$	EOC $(\rho\theta)'$
10	7.508e-11		1.349e+00		1.221e+00		7.508e-11	
20	7.686e-11	-0.0336	1.348e+00	0.0009	1.339e+00	-0.1337	7.686e-11	-0.0336
40	7.728e-11	-0.0079	1.348e+00	0.0000	1.340e+00	-0.0000	7.728e-11	-0.0079
80	7.735e-11	-0.0014	1.411e+00	-0.0660	1.410e+00	-0.0743	7.735e-11	-0.0014
160	1.310e-10	-0.7597	1.725e+00	-0.2901	1.724e+00	-0.2901	1.310e-10	-0.7597

Table 3: Traveling vortex test: EOC for the EXP-RK2 scheme, $CFL = 0.45$, $T = 0.1$

6.2 Test 2: Colliding Pulses

We consider a weakly compressible flow test from [31] with the initial conditions

$$\rho = \bar{\rho} + \varepsilon \left(1 - \cos\left(\frac{2\pi x}{L}\right)\right), \quad \bar{\rho} = 0.955$$
$$u = -\sqrt{\gamma}\,\mathrm{sgn}(x) \left(1 - \cos\left(\frac{2\pi x}{L}\right)\right), \quad \gamma = 1.4$$
$$p = \bar{p} + \varepsilon\gamma \left(1 - \cos\left(\frac{2\pi x}{L}\right)\right), \quad \overline{\rho\theta} = \bar{p} = 1,\ L = 2/\varepsilon$$

and the periodic boundary conditions. The computational domain is $\Omega = [-L, L]$. The initial data, see Figure 5, describe two acoustic pulses: one right-running pulse in the domain $[-L, 0]$ and one left-running pulse in $[0, L]$. The two pulses collide and superimpose in the center of the domain. Their superposition at $T = 0.815$ is shown in Figure 6. Later the pulses separate and shock formation starts due to weakly nonlinear effects, cf. Figure 7 at $T = 1.63$. Analogous behaviour can be seen in Figures 8, 9 for $\varepsilon = 0.001$. Results computed by the IMEX-ARS2 scheme with the CFL numbers $CFL = 0.45$, 2, 4 coincide with the results obtained by the explicit EXP-RK2 scheme with $CFL = 0.45$.

Tables 4 and 5 show the EOC of the IMEX-BDF2 ($CFL_u = 0.3$) and IMEX-ARS2 ($CFL_u = 0.45$) schemes for $\varepsilon = 0.1, 0.01, 0.001$. Since the exact solution is not known, the reference solution is computed on a very fine mesh in order to evaluate the convergence rates (EOC). Note that the initial data are not well-prepared and there are fast acoustic waves present in the solution. As expected our IMEX schemes converge with the second order accuracy, but the convergence order can be recovered only on sufficiently fine meshes, so that fast acoustic waves can be resolved. Numerical experiments presented below confirm this fact.

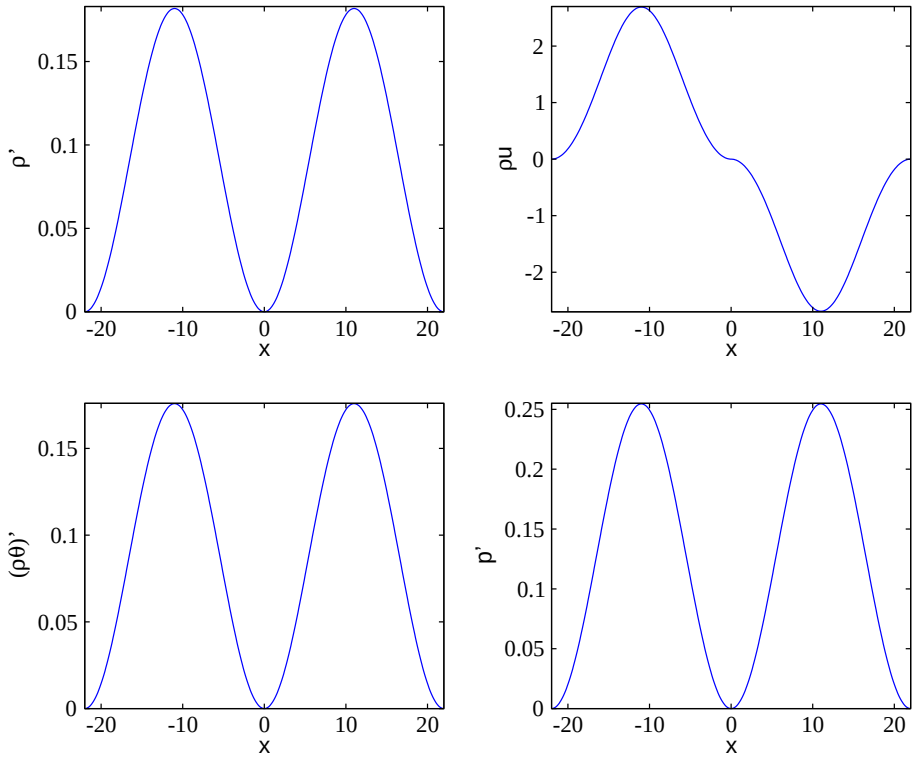

Figure 5: Colliding pulses test, $\varepsilon = 1/11$: initial data

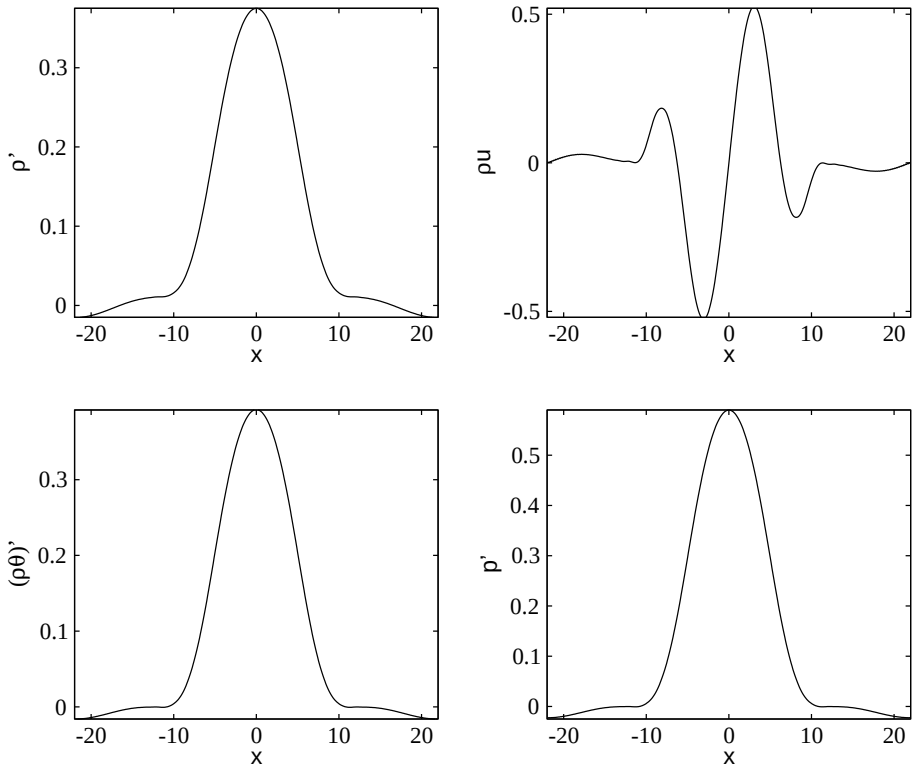

Figure 6: Colliding pulses test, $\varepsilon = 1/11$: solutions obtained by the IMEX-ARS2 scheme with the CFL numbers $CFL = 0.45, 2, 4$ and by the EXP-RK2 scheme with $CFL = 0.45$ on a mesh with 400 cells at time $T = 0.815$

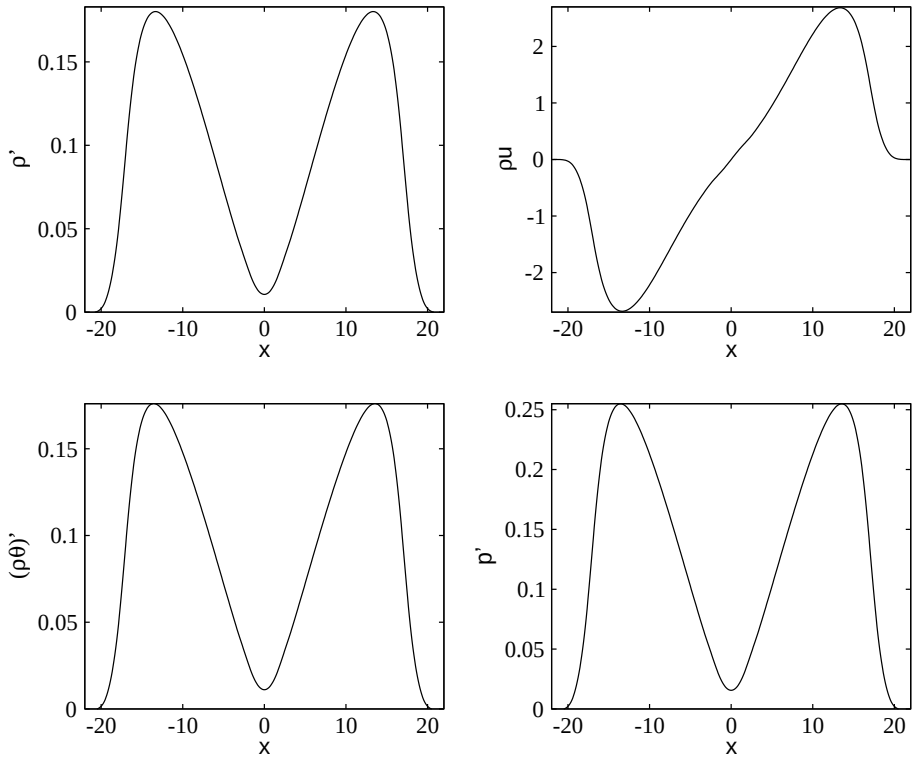

Figure 7: Colliding pulses test, $\varepsilon = 1/11$: solutions obtained by the IMEX-ARS2 scheme with the CFL numbers $CFL = 0.45, 2, 4$ and by the EXP-RK2 scheme with $CFL = 0.45$ on a mesh with 400 cells at time $T = 1.63$

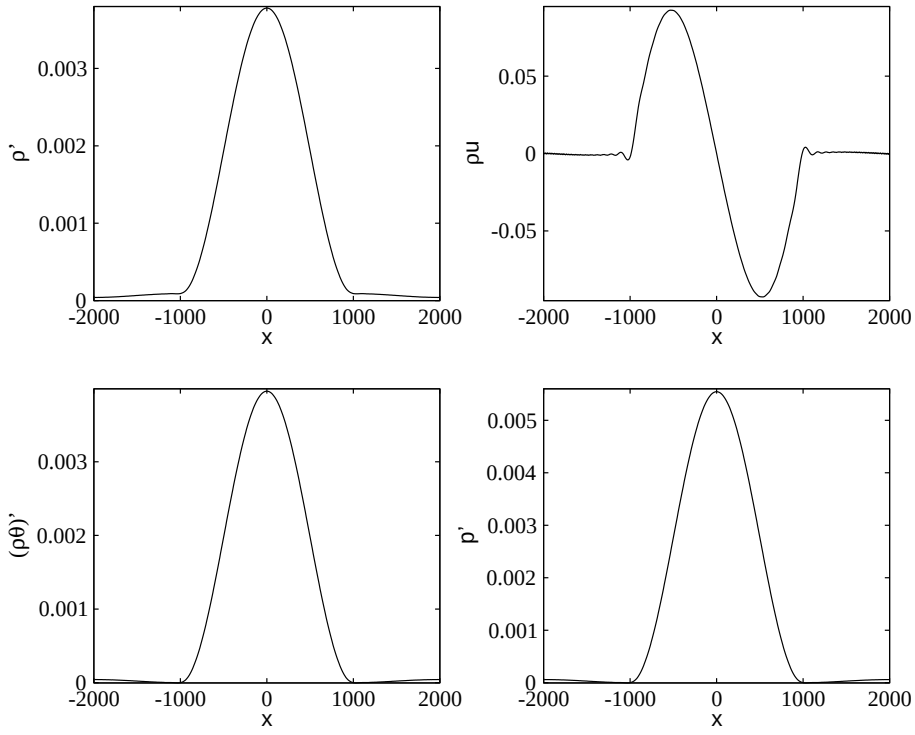

Figure 8: Colliding pulses test, $\varepsilon = 0.001$: solutions obtained by the IMEX-ARS2 scheme with the CFL numbers $CFL = 0.45, 2, 4$ and by the EXP-RK2 scheme with $CFL = 0.45$ on a mesh with 400 cells at time $T = 0.815$

$\varepsilon = 0.1$, $CFL \in [2.7, 18]$

N	L^1-error ρ'	EOC ρ'	L^1-error m	EOC m	L^1-error $(\rho\theta)'$	EOC $(\rho\theta)'$
40	2.509e-01	0.3070	3.11021	1.5760	2.632e-01	0.3224
80	7.290e-02	1.7829	0.99893	1.6386	7.607e-02	1.7906
160	2.454e-02	1.5709	0.35623	1.4876	2.550e-02	1.5765
320	8.093e-03	1.6003	0.11577	1.6216	8.415e-03	1.5997
640	2.547e-03	1.6680	0.03529	1.7138	2.647e-03	1.6684
1280	8.050e-04	1.6616	0.01130	1.6428	8.369e-04	1.6614
2560	2.366e-04	1.7667	0.00336	1.7495	2.463e-04	1.7646
5120	6.265e-05	1.9168	0.00090	1.9046	6.524e-05	1.9166

$\varepsilon = 0.01$, $CFL \in [22, 182]$

N	L^1-error ρ'	EOC ρ'	L^1-error m	EOC m	L^1-error $(\rho\theta)'$	EOC $(\rho\theta)'$
40	2.942e-02	2.2164	4.97053	1.9162	3.061e-02	2.2178
80	8.223e-01	-4.8051	96.70602	-4.2821	8.613e-01	-4.8144
160	2.636e-01	1.6416	51.57914	0.9068	2.758e-01	1.6427
320	8.266e-02	1.6728	21.64870	1.2525	8.653e-02	1.6726
640	2.298e-02	1.8470	7.29348	1.5696	2.405e-02	1.8469
1280	8.569e-03	1.4230	2.94300	1.3093	8.969e-03	1.4231
2560	2.659e-03	1.6886	0.86328	1.7694	2.782e-03	1.6887
5120	8.132e-04	1.7090	0.24643	1.8087	8.508e-04	1.7094

$\varepsilon = 0.001$, $CFL \in [229, 1818]$

N	L^1-error ρ'	EOC ρ'	L^1-error m	EOC m	L^1-error $(\rho\theta)'$	EOC $(\rho\theta)'$
640	6.551e-01	0.0000	756.54660	0.0000	6.860e-01	0.0000
1280	3.634e-01	0.8504	608.20990	0.3149	3.805e-01	0.8505
2560	1.176e-01	1.6278	275.57173	1.1421	1.231e-01	1.6279
5120	3.525e-02	1.7377	111.27334	1.3083	3.691e-02	1.7377
10240	1.139e-02	1.6304	39.72628	1.4859	1.192e-02	1.6304
20480	3.620e-03	1.6534	13.07367	1.6034	3.790e-03	1.6534
40960	1.162e-03	1.6397	4.63654	1.4955	1.216e-03	1.6397
81920	3.689e-04	1.6549	1.20072	1.9492	3.862e-04	1.6549

Table 4: Colliding pulses test: EOC for the IMEX-ARS2 scheme, $CFL_u = 0.45$, $T = 0.815$

$\varepsilon = 0.1$, $CFL \in [1.8, 12]$

N	L^1-error ρ'	EOC ρ'	L^1-error m	EOC m	L^1-error $(\rho\theta)'$	EOC $(\rho\theta)'$
40	2.447e-01	0.8245	4.52910	1.2290	2.618e-01	0.8518
80	1.376e-01	0.8306	2.00780	1.1736	1.446e-01	0.8562
160	6.051e-02	1.1853	0.89010	1.1736	6.343e-02	1.1889
320	1.949e-02	1.6346	0.28626	1.6367	2.035e-02	1.6403
640	6.319e-03	1.6249	0.09305	1.6213	6.608e-03	1.6226
1280	2.402e-03	1.3957	0.03418	1.4448	2.524e-03	1.3887
2560	7.247e-04	1.7286	0.01012	1.7559	7.616e-04	1.7284
5120	2.110e-04	1.7801	0.00293	1.7875	2.220e-04	1.7785

$\varepsilon = 0.01$, $CFL \in [15, 121]$

N	L^1-error ρ'	EOC ρ'	L^1-error m	EOC m	L^1-error $(\rho\theta)'$	EOC $(\rho\theta)'$
40	3.277e-01	-1.2613	45.01215	-1.2625	3.428e-01	-1.2674
80	1.758e-01	0.8982	16.65396	1.4344	1.837e-01	0.9001
160	3.306e-01	-0.9111	51.31600	-1.6235	3.465e-01	-0.9157
320	2.348e-01	0.4937	39.51748	0.3769	2.459e-01	0.4945
640	8.067e-02	1.5414	17.58298	1.1683	8.448e-02	1.5416
1280	2.651e-02	1.6054	7.88240	1.1575	2.778e-02	1.6045
2560	8.124e-03	1.7062	2.90076	1.4422	8.511e-03	1.7066
5120	2.557e-03	1.6678	0.92974	1.6415	2.678e-03	1.6684

$\varepsilon = 0.001$, $CFL \in [153, 1212]$

N	L^1-error ρ'	EOC ρ'	L^1-error m	EOC m	L^1-error $(\rho\theta)'$	EOC $(\rho\theta)'$
640	1.577e-01	-0.9638	142.69328	-0.7552	1.650e-01	-0.9632
1280	4.293e-01	-1.4448	669.35838	-2.2299	4.495e-01	-1.4457
2560	3.149e-01	0.4471	494.63460	0.4364	3.297e-01	0.4472
5120	1.151e-01	1.4519	226.99826	1.1237	1.205e-01	1.4519
10240	3.464e-02	1.7322	97.06844	1.2256	3.628e-02	1.7321
20480	1.007e-02	1.7825	34.57141	1.4894	1.054e-02	1.7826
40960	3.566e-03	1.4978	13.88341	1.3162	3.734e-03	1.4978
81920	1.148e-03	1.6345	4.44900	1.6418	1.203e-03	1.6346

Table 5: Colliding pulses test: EOC for the IMEX-BDF2 scheme, $CFL_u = 0.45$, $T = 0.815$

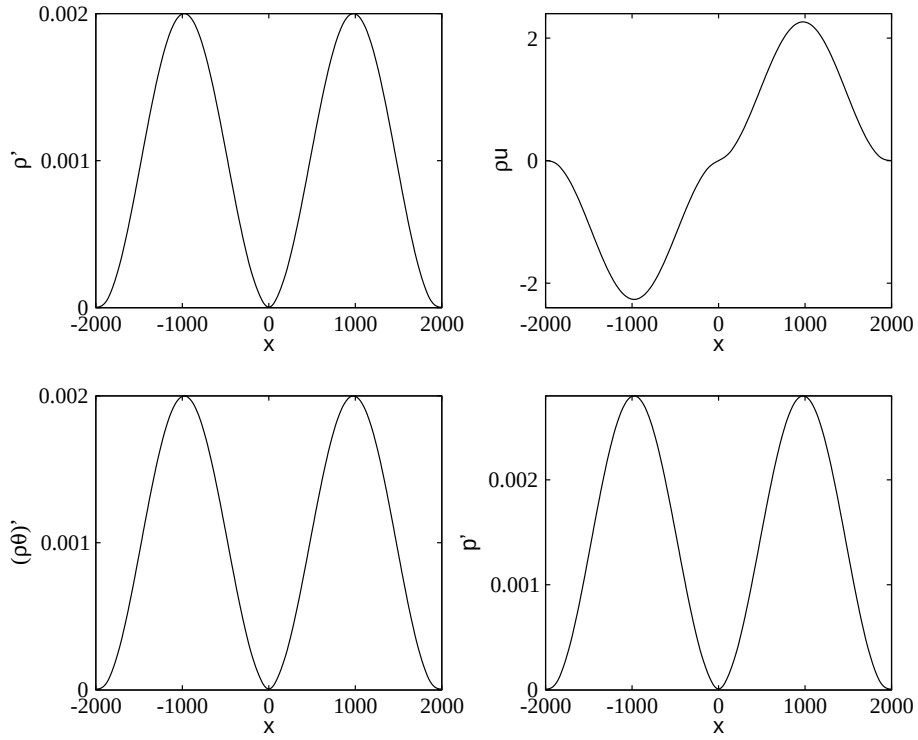

Figure 9: Colliding pulses test, $\varepsilon = 0.001$: solutions obtained by the IMEX-ARS2 scheme with the CFL number $CFL = 0.45$ and by EXP-RK2 scheme with $CFL = 0.45$ on a mesh with 400 cells at time $T = 1.63$

6.3 Test 3: Free Convection of a Smooth Warm Air Bubble

In the following experiment we simulate free convection of a smooth warm air bubble (SWAB) proposed in [22], see also [42]. Initially, a warm air bubble is resting surrounded by cold air. Since the density of the warm air is lower, the bubble rises up due to the buoyancy force. The initial data are

$$\begin{aligned} &\rho' = \frac{p_0}{R}\pi_e^{\frac{1}{\gamma-1}}\left(\frac{1}{\theta}-\frac{1}{\bar{\theta}}\right) = -\bar{\rho}\frac{\theta'}{\theta}, \quad \pi_e = 1-\frac{gy}{c_p\bar{\theta}}, \quad \bar{\rho} = \frac{p_0}{R\bar{\theta}}\pi_e^{\frac{1}{\gamma-1}} \\ &\mathbf{u} = 0 \\ &\theta' = \begin{cases} 0 & r > r_c \\ \frac{\theta'_c}{2}(1+\cos\left(\frac{\pi r}{r_c}\right)) & r \le r_c \end{cases}, \end{aligned} \tag{64}$$

where $\bar{\theta} = 300, \quad p_0 = \bar{p} = 10^5, \quad r_c = 250, \quad \theta'_c = 0.5, \quad r = \|\mathbf{x} - (500, 500, 350)^T\|_2$. Note, that (64) implies that the initial perturbation $(\rho\theta)' = 0$, since $(\rho\theta)' = \rho'\theta + \bar{\rho}\theta' = 0$. Using the reference values $x_{ref} = 1000$m, $t_{ref} = 1000$s, $u_{ref} = 1$m/s, $p_{ref} = R\rho_{ref}\theta_{ref}$ we have

$$\varepsilon^2 = \frac{u_{ref}^2}{x_{ref}g} = \frac{u_{ref}^2\rho_{ref}}{p_{ref}} = \frac{u_{ref}^2}{R\theta_{ref}}$$

and consequently $\theta_{ref} = \frac{u_{ref}^2}{R\varepsilon^2} = \varepsilon^{-2}/R$. Thus, the non-dimensional initial data read

$$\begin{aligned}
&\theta' = \begin{cases} 0 & r > r_c \\ \frac{\theta_c'}{2}(1+\cos\left(\frac{\pi r}{r_c}\right)) & r \le r_c \end{cases}, \quad r = \|\mathbf{x} - (0.5, 0.5, 0.35)^T\|_2, \\
&r_c = 0.25, \quad \theta_c' = \frac{1}{2\theta_{ref}} = \frac{R\varepsilon^2}{2}, \\
&\rho' = -\frac{\bar\rho\theta'}{\theta}, \quad \bar\theta = 1, \quad \bar\rho = \left(1 - \frac{\gamma-1}{\gamma}x_3\right)^{\frac{1}{\gamma-1}}.
\end{aligned} \tag{65}$$

In this experiment it is reasonable to apply no-flux boundary conditions $\mathbf{u}\cdot\mathbf{n} = 0$, $\nabla(\bar c^2(\rho\theta)')\cdot\mathbf{n} = 0$, $\nabla\rho'\cdot\mathbf{n} = 0$. Note, that these boundary conditions are reflected in the system matrix A in (29) and most importantly in the matrix E in (32). Let us highlight the fact that different boundary conditions are used for $\mathbf{u}$ and $(\rho\theta)'$, ρ', respectively, by $\mathfrak{D}^u_{x_j}$ and $\mathfrak{D}^p_{x_j}$, $j = 1, 2, 3$. Consequently, we have the following discrete equations for the momentum, cf. (31)

$$\begin{aligned}
\mathbf{Q}_j^{n+1} &= \hat{\mathbf{Q}} - \frac{\Delta t}{\varepsilon^2}\mathfrak{D}^p_{x_j}\bar C^2\bar\Theta^{-1}(\boldsymbol{\rho\theta})'^{n+1}, \quad j = 1, 2, \\
\mathbf{Q}_3^{n+1} &= \hat{\mathbf{Q}} - \frac{\Delta t}{\varepsilon^2}\mathfrak{D}^p_{x_3}\bar C^2\bar\Theta^{-1}(\boldsymbol{\rho\theta})'^{n+1} - \frac{\Delta t}{\varepsilon^2}\boldsymbol{\rho}'^{n+1}
\end{aligned}$$

and for the potential temperature, cf. (32)

$$\left[\mathbb{1} - \frac{\Delta t^2}{\varepsilon^2}E\right](\boldsymbol{\rho\theta})'^{n+1} = (\hat{\boldsymbol{\rho\theta}})' - \Delta t\bar\Theta\nabla_h^u\cdot\hat{\mathbf{Q}} - \frac{\Delta t^2}{\varepsilon^2}\mathfrak{D}^u_{x_3}((\hat{\boldsymbol{\rho\theta}})' - \bar\Theta\boldsymbol{\rho}'), \tag{66}$$

where

$$E = \Delta_h^p\bar C^2 + \mathfrak{D}^u_{x_3}, \quad \Delta_h^p = \sum_{i=1}^{3}\mathfrak{D}^u_{x_i}\mathfrak{D}^p_{x_i}. \tag{67}$$

6.3.1 One-dimensional case

Firstly, we consider one-dimensional setting, which allows us to compute a numerical solution using sufficiently fine mesh resolution. We set the computational domain Ω to $[0, 1]$, place the center of warm air bubble at $x = 0.5$ and use no-flux boundary conditions. The solution shows the following behaviour: in the beginning the potential temperature and velocity evolve quite rapidly, while the density is changing only slowly. Then the solution changes in a periodic pattern on a fast time scale. Let us note that the solution dynamics in one space dimension differs substantially from the multi-dimensional situation. Nevertheless, we can use this test case to analyse the accuracy and the experimental order of convergence with respect to ε and CFL numbers. Due to the presence of the fast waves we obtain the second order convergence rates only for relatively fine grids if the CFL_u stability condition (25) is used, see Tables 6 and 7. On the other hand, Tables 8 and 9 demonstrate that under a slight control of the whole CFL number (26), e.g. $CFL = 8$, the second order accuracy can be recovered on coarser meshes. In Tables 7 and 9 we present the experimental order of convergence using the weighted norms $\|\bar c\rho'/\varepsilon\|_{L^2(\Omega)}$, $\|m\|_{L^2(\Omega)}$ and $\|\bar c(\rho\theta)'/(\bar\theta\varepsilon)\|_{L^2(\Omega)}$ that follows from the stability analysis, cf. Section 5. We can clearly notice higher convergence rates with respect to these energy-related norms.

6.3.2 Multi-dimensional case

In this experiment we will consider three-dimensional rising air bubble test (64). The initial data and the numerical solution obtained by the three-dimensional simulations using the IMEX-

$\varepsilon = 0.01$

N	L^1-error ρ'	EOC ρ'	L^1-error m	EOC m	L^1-error $(\rho\theta)'$	EOC $(\rho\theta)'$
640	2.880e-04	0.1456	3.990e-03	2.3115	2.912e-04	0.1436
1280	9.598e-05	1.5853	1.619e-02	-2.0207	9.611e-05	1.5993
2560	4.233e-05	1.1812	6.076e-03	1.4138	4.236e-05	1.1819
5120	1.307e-05	1.6948	1.267e-03	2.2620	1.309e-05	1.6946
10240	3.552e-06	1.8799	2.764e-04	2.1965	3.554e-06	1.8808
20480	8.899e-07	1.9970	6.526e-05	2.0823	8.901e-07	1.9974

$\varepsilon = 0.001$

N	L^1-error ρ'	EOC ρ'	L^1-error m	EOC m	L^1-error $(\rho\theta)'$	EOC $(\rho\theta)'$
10240	1.736e-06	2.8347	5.040e-03	-0.5310	1.736e-06	2.8348
20480	1.153e-06	0.5907	3.316e-03	0.6039	1.153e-06	0.5906
40960	1.620e-06	-0.4914	1.124e-03	1.5610	1.621e-06	-0.4915
81920	4.354e-07	1.8959	5.439e-04	1.0471	4.354e-07	1.8960
163840	6.547e-08	2.7335	1.654e-04	1.7176	6.547e-08	2.7334
327680	1.873e-08	1.8058	4.274e-05	1.9521	1.873e-08	1.8058

Table 6: SWAB 1D test: EOC for the IMEX-ARS2 scheme, $CFL_u = 0.45$, $T = 0.05$

$\varepsilon = 0.01$

N	L^2-error $\bar{c}\rho'/\varepsilon$	EOC	L^2-error m	EOC	L^2-error $\bar{c}(\rho\theta)'/(\theta\varepsilon)$	EOC
640	1.439e-03	0.8225	1.842e-04	2.8751	1.455e-03	0.8091
1280	3.243e-04	2.1495	5.206e-04	-1.4986	3.249e-04	2.1630
2560	1.070e-04	1.6001	1.400e-04	1.8951	1.070e-04	1.6022
5120	2.567e-05	2.0593	2.481e-05	2.4960	2.567e-05	2.0594
10240	5.075e-06	2.3385	4.172e-06	2.5721	5.075e-06	2.3387
20480	9.306e-07	2.4473	7.261e-07	2.5226	9.306e-07	2.4473

$\varepsilon = 0.001$

N	L^2-error $\bar{c}\rho'/\varepsilon$	EOC	L^2-error m	EOC	L^2-error $\bar{c}(\rho\theta)'/(\theta\varepsilon)$	EOC
10240	1.979e-05	3.1364	5.239e-05	0.0156	1.979e-05	3.1365
20480	8.333e-06	1.2480	2.690e-05	0.9614	8.334e-06	1.2479
40960	8.121e-06	0.0372	6.512e-06	2.0468	8.122e-06	0.0372
81920	1.663e-06	2.2878	2.503e-06	1.3794	1.663e-06	2.2879
163840	1.938e-07	3.1012	5.716e-07	2.1304	1.938e-07	3.1012
327680	3.855e-08	2.3297	1.020e-07	2.4870	3.855e-08	2.3297

Table 7: SWAB 1D test: EOC for the IMEX-ARS2 scheme, $CFL_u = 0.45$, $T = 0.05$

$\varepsilon = 0.01$, $CFL = 8$

N	L^1-error ρ'	EOC ρ'	L^1-error m	EOC m	L^1-error $(\rho\theta)'$	EOC $(\rho\theta)'$
320	1.680e-05	1.6495	1.654e-03	2.1858	1.680e-05	1.6534
640	4.470e-06	1.9102	3.777e-04	2.1309	4.468e-06	1.9113
1280	1.148e-06	1.9613	9.155e-05	2.0446	1.148e-06	1.9608
2560	2.846e-07	2.0121	2.237e-05	2.0330	2.844e-07	2.0126
5120	7.009e-08	2.0215	5.852e-06	1.9344	6.994e-08	2.0239

$\varepsilon = 0.001$, $CFL = 8$

N	L^1-error ρ'	EOC ρ'	L^1-error m	EOC m	L^1-error $(\rho\theta)'$	EOC $(\rho\theta)'$
320	1.177e-06	-0.4086	1.645e-03	1.3203	1.177e-06	-0.4083
640	2.954e-07	1.9942	6.658e-04	1.3048	2.954e-07	1.9942
1280	5.906e-08	2.3225	2.236e-04	1.5744	5.907e-08	2.3224
2560	1.686e-08	1.8087	6.226e-05	1.8445	1.686e-08	1.8089
5120	4.245e-09	1.9898	1.616e-05	1.9461	4.244e-09	1.9898

Table 8: SWAB 1D test: EOC for the IMEX-ARS2 scheme, $T =$ 0.05

$\varepsilon = 0.01$

N	L^2-error $\bar{c}\rho'/\varepsilon$	EOC	L^2-error m	EOC	L^2-error $\bar{c}(\rho\theta)'/(\theta\varepsilon)$	EOC
320	1.264e-04	2.0085	1.275e-04	2.4349	1.264e-04	2.0130
640	2.551e-05	2.3095	2.170e-05	2.5545	2.549e-05	2.3098
1280	4.767e-06	2.4197	3.817e-06	2.5076	4.764e-06	2.4196
2560	8.765e-07	2.4434	6.970e-07	2.4531	8.758e-07	2.4434
5120	1.630e-07	2.4271	1.327e-07	2.3934	1.629e-07	2.4271

$\varepsilon = 0.001$

N	L^2-error $\bar{c}\rho'/\varepsilon$	EOC	L^2-error m	EOC	L^2-error $\bar{c}(\rho\theta)'/(\theta\varepsilon)$	EOC
320	8.082e-05	0.1267	1.126e-04	1.8214	8.082e-05	0.1272
640	1.667e-05	2.2772	3.234e-05	1.7995	1.667e-05	2.2772
1280	2.249e-06	2.8899	7.249e-06	2.1575	2.250e-06	2.8898
2560	4.542e-07	2.3081	1.395e-06	2.3770	4.543e-07	2.3081
5120	8.606e-08	2.4000	2.542e-07	2.4568	8.606e-08	2.4001

Table 9: SWAB 1D test: EOC for the IMEX-ARS2 scheme, $CFL = 8$, $T =$ 0.05

N	L^1-error $\mathbf{w}$	EOC $\mathbf{w}$	L^1-error m_1	EOC m_1	L^1-error m_3	EOC m_3	L^1-error θ'	EOC θ'
32	3.296e-03	2.0487	6.662e-03	2.0944	6.480e-03	2.0025	1.809e-03	1.6086
64	7.967e-04	2.0194	1.560e-03	2.0152	1.617e-03	2.0248	5.932e-04	1.7868
128	1.965e-04	1.8050	3.859e-04	1.7343	3.974e-04	1.8836	1.719e-04	2.0539
256	5.624e-05	1.9046	1.160e-04	1.9570	1.077e-04	1.8810	4.140e-05	2.0227
512	1.502e-05	1.3961	2.987e-05	1.8213	2.924e-05	1.1223	1.019e-05	2.3914

Table 10: SWAB quasi-3D test: EOC of IMEX-BDF2 scheme, $T = 0.15$, $CFL_u = 0.4$, $CFL \in [2.8, 300]$, $\varepsilon = 0.01$.

N	L^1-error $\mathbf{w}$	EOC $\mathbf{w}$	L^1-error m_1	EOC m_1	L^1-error m_3	EOC m_3	L^1-error θ'	EOC θ'
32	9.470e-03	1.0416	1.862e-02	1.0563	1.859e-02	1.0673	1.556e-03	0.9429
64	4.601e-03	0.9944	8.953e-03	1.0304	8.871e-03	1.0396	8.094e-04	1.0475
128	2.309e-03	0.9993	4.383e-03	1.0949	4.315e-03	1.0823	3.916e-04	1.1047
256	1.155e-03	0.9381	2.052e-03	1.2167	2.038e-03	1.0339	1.821e-04	1.2251
512	6.029e-04	0.8246	8.830e-04	1.5853	9.953e-04	1.2301	7.790e-05	1.5804

Table 11: SWAB quasi-3D test: EOC of IMEX-ARS2 scheme, $T = 0.15$, $CFL_u = 0.4$, $CFL \in [2.8, 300]$, $\varepsilon = 0.01$.

BDF2 scheme are shown in Figure 10. In tables Table 10 and 11 the experimental order of convergence was obtained by means of quasi-3D simulations, see Figure 11. To reduce CPU time these experiments were performed in a 3D-box in which the x_2-direction consists of one layer of cells whereas each of the x_1 and x_3 directions consists of N layers of cells. Numerical experiments clearly demonstrate the expected second order accuracy even on relatively coarse grids for the IMEX-BDF2 scheme. Note that the convergence of the IMEX-ARS2 scheme is slightly worse for this test case, as shown in Table 11.

6.4 Test 4: Inertia-gravity waves

The inertia-gravity waves experiment has been taken from [22]. The initial conditions have been proposed firstly in [53]. The background state is a uniformly stratified atmosphere with a Brunt-Väisälä frequency

$$\mathcal{N} = g\frac{d}{dy}(\ln\bar{\theta})$$

which yields the background potential temperature

$$\bar{\theta} = \theta_0 \exp\left(\frac{\mathcal{N}^2}{g}y\right).$$

The Exner pressure obtained from the hydrostatic balance yields in this case

$$\bar{\pi} = 1 + \frac{g^2}{c_p\theta_0\mathcal{N}^2}\left(\exp\left(-\frac{\mathcal{N}^2}{g}y\right) - 1\right).$$

The perturbation of the potential temperature is given by

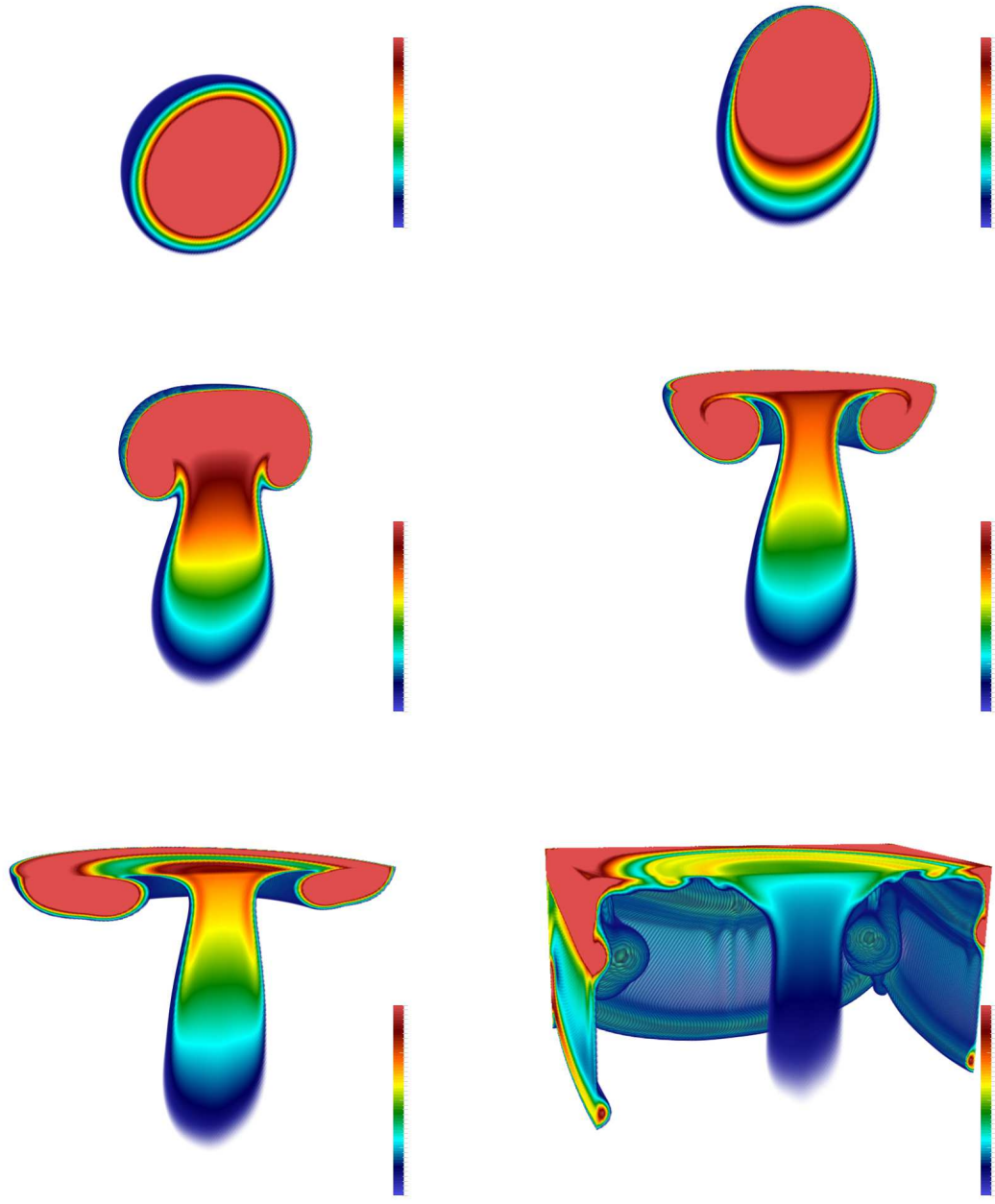

Figure 10: SWAB 3D test, $\varepsilon = 0.01$: IMEX-BDF2 scheme, for times (from left to right, top to bottom) $t = 0$, 0.3, 0.5, 0.6, 0.7, 1.1, with mesh resolution $\Delta x_1 = \Delta x_2 = \Delta x_3 = 1/128$, $CFL_u = 0.4$, $CFL \in [27, 200]$. Only a half of the computational domain is shown in the x_1-direction to visualize the interior temperature profiles. Colors correspond to the potential temperature θ' in the range $0 - 0.1$K. The background color ($\theta' = 0$) has been removed.

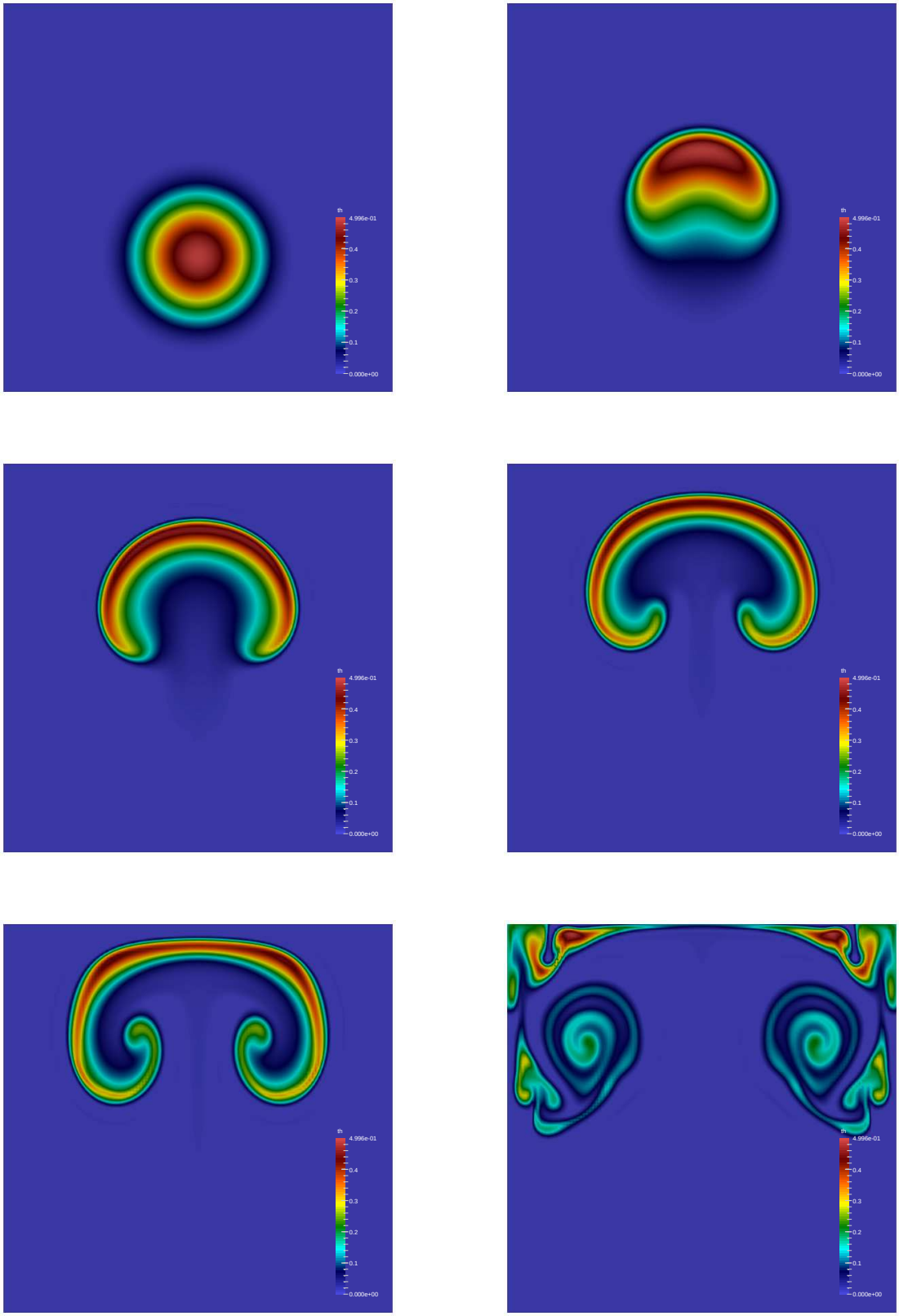

Figure 11: SWAB quasi-3D test, $\varepsilon = 0.01$: IMEX-BDF2 scheme, for times (from left to right, top to bottom) $t = 0$, 0.3, 0.5, 0.6, 0.7, 1.1, with mesh resolution $\Delta x_1 = \Delta x_2 = \Delta x_3 = 1/128$, $CFL_u = 0.4$, $CFL \in [27, 200]$. The $x_1 - x_3$ planes illustrate time evolution of the interior temperature profiles of a three-dimensional system containing one cell layer in the x_2-direction. Colors correspond to the potential temperature θ' in the range $0 - 0.5$K.

$$\theta' = \theta_c \frac{\sin\left(\frac{\pi_c y}{h_c}\right)}{1 + \left(\frac{x - x_c}{a_c}\right)^2},$$

where $\theta_c = 0.01$K, $\theta_0 = 300$K, $h_c = 10$km, $a_c = 5$km, $x_c = 100$km, and $\mathcal{N} = 0.01\text{s}^{-1}$. The domain size in the (x_1, x_2, x_3) directions is 300km×0.25km×10km. We use periodic and no-flux boundary conditions for the horizontal and vertical directions, respectively. This initial state is advected horizontally with a constant velocity $\bar{u} = 20$m/s.

Figure 12 shows the excess potential temperature for the Lax-Friedrichs flux models obtained after 3000s on regular grids with the resolution 250m calculated using dimensional formulation of the Euler equations (4). The global extreme values of the results are in the range $\theta' = [-0.001772,\ 0.003379]$ and $w = [-0.0102006,\ 0.014102]$. The result demonstrates that the IMEX finite volume method can be successfully applied to compute internal gravity waves in the non-homentropic case, that is, when the background potential temperature is non-constant. Note that the results with/without the non-linear pressure perturbation p'_{NL} are similar (see Figure 12).

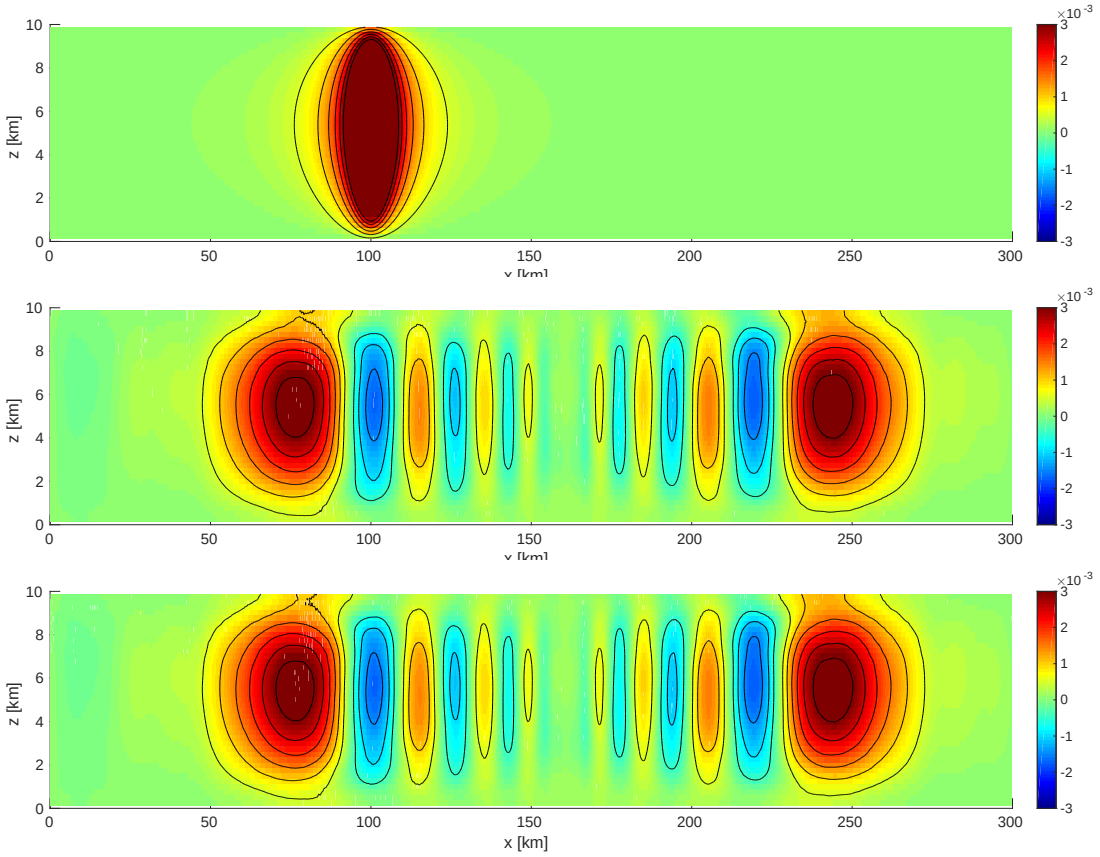

Figure 12: Inertia-gravity wave quasi-3D test using the Euler equations (4) with $\varepsilon \approx 0.06$ computed by the IMEX-ARS2 method with the Lax-Friedrichs flux. Top: initial data for the potential temperature θ'; middle: θ' at time $t = 3000$s using only the linear pressure perturbation, p'_L; bottom: θ' at time $t = 3000$s using also the non-linear pressure perturbation, p'_{NL}, in the non-linear operator. Mesh resolution $\Delta x_1 = \Delta x_2 = \Delta x_3 = 1/4$, $CFL_u = 0.4$, $CFL \approx 7$. Colors correspond to the potential temperature θ' in the range $[-0.003\ 0.003]$K, contour levels are shown for the values $[-0.0015\ 0.003]$K by the step 0.0005K.

7 Conclusions

In the present paper we have derived and analysed asymptotic preserving IMEX FV methods for low Mach number flows with gravitation. The compressible Euler equations (1) are governed by hyperbolic balance laws describing the evolution of density, momentum and potential temperature. This system is often used in meteorology in order to model stratified fluid flows. In the low Mach number regime, which is typical for meteorological applications, the resulting system has a multiscale character. In order to efficiently approximate slow advective flows, we split the full nonlinear system into the linear and nonlinear operators. The stiff linear operator models the linearized acoustic and gravity waves, whereas the non-stiff nonlinear operator represents the advective transport. For spatial discretization we apply the finite volume method with suitable numerical fluxes. Thus, to avoid numerical diffusion in the linear waves the central difference fluxes are used. On the other hand, we can apply any suitable numerical flux, that is used for hyperbolic conservation laws, in order to approximate the nonlinear operator. In this paper we have used the Rusanov or the Lax-Friedrichs method. For time discretization second order globally stiffly accurate IMEX methods are applied: the stiff linear operator is approximated implicitly and the nonlinear non-stiff operator explicitly in time.

In Sections 4 and 5 we have proved that the proposed IMEX FV methods are asymptotic preserving in the sense that they are uniformly consistent and stable for any $0 < \varepsilon << 1$. Moreover, our schemes preserve the hydrostatic equilibrium state in the following sense: if $\mathbf{w}^n = \mathbf{0}$, then also $\mathbf{w}^{n+1} = \mathbf{0}$. Consequently, they are also well-balanced. A series of one-, two- and three-dimensional numerical experiments confirm the asymptotic preserving property of the derived IMEX FV schemes. Indeed, if the advective effects are dominant we obtain the second order convergence rate uniformly with respect to ε.

Acknowledgements

This work has been supported by the German Science Foundation under the grants LU 1470/2-3 and the Collaborative Research Centers TRR 146 and TRR 165. The authors wish to thank E. Feireisl (Praha), R. Klein (Berlin) and S. Noelle (Aachen) for fruitful discussions on the topic. The authors further acknowledge the support of the Center for Data Processing (ZDV) of the Johannes Gutenberg-University Mainz.

References

[1] A. S. Almgren, J. B. Bell, C. A. Rendleman, and M. Zingale, *Low Mach number modeling of type Ia supernovae. I. hydrodynamics*, Astrophys. J., 637 (2006), 922–936.

[2] U.M. Ascher, S.J. Ruuth, and R.J. Spiteri, *Implicit-explicit Runge-Kutta methods for time-dependent partial differential equations*, Appl. Numer. Math., 25(2-3) (1997), pp. 151–167.

[3] U.M. Ascher, S.J. Ruuth, and B.T.R. Wetton, *Implicit-explicit methods for time-dependent partial differential equations*, J. Numer. Anal., 32(3) (1995), pp. 797–823.

[4] E. Audusse, F. Bouchut, M. Bristeau, R. Klein, and B. Perthame, *A fast and stable well-balanced scheme with hydrostatic reconstruction for shallow water flows*, SIAM J. Sci. Comput., 25(6) (2004), pp. 2050–2065.

[5] T. Benacchio, W. O'Neill, and R. Klein, *A blended soundproof-to-compressible model for atmospheric dynamcis*, Mon. Wea. Rev., 142 (2014), pp. 4416–4438.

[6] H. Bijl and P. Wesseling, *A unified method for computing incompressible and compressible flows in boundary-fitted coordinates*, J. Comput. Phys., 141(2) (1998), pp. 153–173.

[7] G. Bispen, *IMEX finite volume schemes for the shallow water equations*, PhD-thesis, 2015.

[8] G. Bispen, K. R. Arun, M. Lukáčová-Medviďová, and S. Noelle, *IMEX large time step finite volume methods for low Froude number shallow water flows*, Comm. Comput. Phys., 16 (2014), pp. 307–347.

[9] G. Bispen, K. R. Arun, M. Lukáčová-Medviďová, and L. Yelash, *IMEX finite volume evolution Galerkin schemes for three-dimensional weakly compresible flows*, Proceedings of Algoritmy, Eds. K. Mikula et al., (2016).

[10] N. Botta, R. Klein, S. Langenberg, and S. Lützenkirchen, *Well balanced finite volume methods for nearly hydrostatic flows,* J. Comput. Phys., 196(2) (2004), pp. 539–565.

[11] A. Canestrelli, M. Dumbser, A. Siviglia, and E.F. Toro, *Well-balanced high-order centered schemes on unstructured meshes for shallow water equations with fixed and mobile bed*, Advanced in Water Resources, 33(2010), pp. 291–303.

[12] P. Chandrashekar and C. Klingenberg, *A second order well-balanced finite volume scheme for Euler equations with gravity*, SIAM J. Sci. Comput. 37 (2015), pp. B382–B402.

[13] A. Chertock, S. Cui, A. Kurganov, S. Ozcan, and E. Tadmor, *Well-balanced central-upwind schemes for the Euler equations with gravitation*, submitted, (2015).

[14] P.G. Ciarlet, *The Finite Element Method for Elliptic Problems*, North-Holland, Amsterdam, (1978).

[15] P. J. Davis, *Circulant Matrices. 2nd ed.*, New York, NY: AMS Chelsea Publishing, (1994).

[16] T. A. Davis, *Algortihm 832: UMFPACK v4.3-an unsymmetric-pattern multifrontal method*, ACM Trans. Math. Softw., 30(2) (2004), pp. 196–199.

[17] P. Degond and M. Tang, *All speed scheme for the low Mach number limit of the isentropic Euler equations*, Commun. Comput. Phys., 10(1) (2011), pp. 1–31.

[18] E. Feireisl and A. Novotný, *Inviscid incompressible limits of the full Navier-Stokes-Fourier system*, Commun. Math. Phys., 321 (2013), pp. 605–628.

[19] E. Feireisl, R. Klein, A. Novotný, and E. Zatorska, *On singular limits arising in the scale analysis of stratified fluid flows*, Math. Models Methods Appl. Sci., 26 (3) (2016), pp. 419–443.

[20] M. Feistauer, V. Dolejší, and V. Kučera, *On the discontinuous Galerkin method for the simulation of compressible flow with wide range of Mach numbers*, Computing and Visualization in Science, 10 (2007), pp. 17–27.

[21] M. Feistauer and V. Kučera, *On a robust discontinuous Galerkin technique for the solution of compressible flow*, J. Comput. Phys., 224 (2007), pp. 208–221.

[22] F.X. Giraldo and M. Restelli, *A study of spectral element and discontinuous Galerkin methods for the Navier-Stokes equations in nonhydrostatic mesoscale atmospheric modeling: equation sets and test cases*, J. Comput. Phys., 227 (2008), pp. 3849–3877.

[23] F.X. Giraldo, M. Restelli, and M. Lauter, *Semi-implicit formulations of the Navier–Stokes equations: application to nonhydrostatic atmospheric modeling*, SIAM J. Sci. Comput., 32 (2010), pp. 3394–3425.

[24] G. H. Golub and C. V. Van Loan, *Matrix computations. 4th ed.*, Baltimore, MD: The Johns Hopkins University Press, (2013).

[25] J. Haack, S. Jin, and J.-G. Liu, *An all-speed asymptotic-preserving method for the isentropic Euler and Navier-Stokes equations*, Commun. Comput. Phys., 12 (2012), pp. 955–980.

[26] D.R. van der Heul, C. Viuk, and P. Wesseling, *A conservative pressure-correction method for flow at all speeds* Computers & Fluids, 32(8) (2003), pp. 1113–1132.

[27] J. Jang, F. Li, J.-M. Qiu, and T. Xiong, *Analysis of asymptotic preserving DG-IMEX schemes for linear kinetic transport equations in a diffusive scaling*, SIAM J. Numer. Anal., 52(4), (2014), pp. 2048–2072.

[28] S. Jin, *Asymptotic preserving (AP) schemes for multiscale kinetic and hyperbolic equations: a review*, Riv. Mat. Univ. Parma, 3 (2012), pp. 177–216.

[29] K. Kaiser, J. Schütz, R. Schöbel, and S. Noelle, *A new stable splitting for the isentropic Euler equations*, IGPM report 442, RWTH Aachen University (2016).

[30] S. Klainerman and A. Majda, *Singular limits of quasilinear hyperbolic systems with large parameters and the incompressible limit of compressible fluids*, Comm. Pure Appl. Math., 34(4) (1981), pp. 481–524.

[31] R. Klein, *Semi-implicit extension of a Godunov-type scheme based on low Mach number asymptotics I. One-dimensional flow*, J. Comput. Phys., 121(2) (1995), pp. 213–237.

[32] R. Klein, *An applied mathematical view of meteorological modelling*, Hill, James M. (ed.) et al., Applied mathematics entering the 21st century. Papers from the 5th international congress on industrial and applied mathematics (ICIAM 2003), Sydney, Australia, July 7–11, 2003. Philadelphia, PA: Society for Industrial and Applied Mathematics (SIAM). Proceedings in Applied Mathematics, 116 (2004), pp. 227-269.

[33] R. Klein, *Asymptotic analyses for atmospherics flows and the construction of asymptotically adaptive numerical methods*, Zeitschr. Angew. Math. Mech., 80 (2000), pp. 765–777.

[34] R. Klein, *Asymptotics, structure, and integration of sound-proof atmospheric flow equations*, Theor. & Comput. Fluid Dyn., 23(3) (2009), pp. 161–195.

[35] R. Klein, U. Achatz, D. Bresch, O.M. Knio, and P.K. Smolarkiewicz, *Regime of Validity of Sound-Proof Atmospheric Flow Models*, J. Atmos. Sci., 67 (2010), pp. 3226–3237.

[36] R. Klein and T. Benacchio, *A doubly blended model for multiscale atmospheric dynamics*, J. Atmos. Sci., available online (2016).

[37] M. Lukáčová-Medviďová, S. Noelle, and M. Kraft, *Well-balanced finite volume evolution Galerkin methods for the shallow water equations.* J. Comput. Phys., 221(1) (2007), pp. 122–147.

[38] M. Lukáčová-Medviďová, and K.W. Morton, *Finite volume evolution Galerkin methods—a survey*, Indian J. Pure Appl. Math., 41 (2010), pp. 329–361.

[39] M. Lukáčová-Medviďová, K.W. Morton, and G. Warnecke, *Finite volume evolution Galerkin methods for hyperbolic systems*, J. Sci. Comput., 26(1) (2004), pp. 1–30.

[40] M. Lukáčová Medviďová, A. Müller, V. Wirth, and L. Yelash, *Adaptive discontinuous evolution Galerkin method for dry atmospheric flow.* J. Comput. Phys., 268 (2014), pp. 106–133.

[41] C.-D. Munz, S. Roller, R. Klein, and K.J. Geratz, *The extension of incompressible flow solvers to the weakly compressible regime* Computers & Fluids, 32(2) (2003), pp. 173–196.

[42] A. Müller, J. Behrens, F.X., Giraldo, and V. Wirth, *Comparison between adaptive and uniform discontinuous Galerkin simulations in dry 2D bubble experiments*, J. Comput. Phys., 235 (2013), pp. 371–393.

[43] S. Noelle, G. Bispen, K.R. Arun, M. Lukáčová-Medviďová, and C.-D. Munz, *A weakly asymptotic preserving low Mach number scheme for the Euler equations of gas dynamics*, SIAM J. Sci. Comput., 36(6) (2014), pp. 989–1024.

[44] Y. Ogura and N. Phillips, *Scale analysis for deep and shallow convection in the atmosphere*, J. Atmos. Sci., 19 (1962), pp. 173–179.

[45] J. H. Park and C.-D. Munz, *Multiple pressure variables methods for fluid flow at all Mach numbers*, Internat. J. Numer. Methods Fluids, 49(8) (2005), pp. 905–931.

[46] M. Restelli, *Semi-Lagrangian and Semi-Implicit Discontinuous Galerkin Methods for Atmospheric Modeling Applications*, PhD thesis, Politecnico di Milano, (2007).

[47] M. Restelli and F.X. Giraldo, *A conservative discontinuous Galerkin semi-implicit formulation for the Navier–Stokes equations in nonhydrostatic mesoscale modeling*, SIAM J. Sci. Comput., 31 (2009), pp. 2231–2257.

[48] M. Ricchiuto and A. Bollermann, *Stabilized residual distribution for shallow water simulations*, J. Comput. Phys., 228(4) (2009), pp. 1071–1115.

[49] P.K. Smolarkiewicz, C. Kühnlein, and N.P. Wedi, *A consistent framework for discrete integrations of soundproof and compressible PDEs of atmospheric dynamics*, J. Comput. Phys., 263 (2014), pp. 185–205.

[50] Y. Sun and Y.-X. Ren, *The finite volume local evolution Galerkin method for solving the hyperbolic conservation laws*, J. Comput. Phys., 228(13) (2009), pp. 4945–4960.

[51] S. Thomas, C. Girard, G. Doms, and U. Schattler, *Semi-implicit scheme for the DWD Lokal-Modell*, Meteorol. Atmos. Phys. 73 (2000), pp. 105–125.

[52] R.K. Zeytounian, *Meteorological Fluid Dynamics, Lecture Notes in Physics*, m5., Springer, (1991).

[53] W.C. Skamarock and J.B. Klemp *Efficiency and accuracy of the Klemp–Wilhelmson time-splitting technique*, Monthly Weather Review 122 (1994), pp. 2623–2630.